Applied Thermal Engineering 247 (2024) 122961

Contents lists available at ScienceDirect

Applied Thermal Engineering

journal homepage: www.elsevier.com/locate/apthermeng

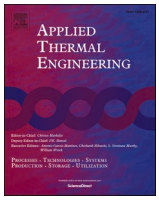

Research Paper

Experimental and numerical investigation of a novel high-temperature heat pump for sensible and latent heat delivery

Miguel Ramirez [a,d,*], Felipe Trebilcock-Kelly [a], José L. Corrales-Ciganda [a], Jorge Payá [b], Abdelrahman H. Hassan [b,c]

[a] TECNALIA, Basque Research and Technology Aliance (BRTA), Area Anardi 5, Azpeitia, Guipuzkoa 20730, Spain
[b] Instituto Universitario de Investigación en Ingeniería Energética (IIE), Universitat Politècnica de València (UPV), Valencia 46022, Spain
[c] Mechanical Power Engineering Department, Faculty of Engineering, Zagazig University, Zagazig 44519, Egypt
[d] TNO, Sustainable Technologies for Industrial Processes Unit, Westerduinweg 3, 1755 LE Petten, The Netherlands

ARTICLE INFO

Keywords:
High-temperature heat pump
Subcooler
Piston-compressor
Heat recovery
R-1233zd(E)
Numerical modeling

ABSTRACT

This paper investigates, both experimentally and numerically, the performance of a high-temperature heat pump (HTHP) prototype for steam production and thermal energy storage applications using R-1233zd(E) as a refrigerant. The main novelties of this prototype are the incorporation of an external subcooler to separate the sensible and latent heat production. Other novel points are the testing of a new variable-speed piston compressor that endures a discharge temperature of up to 160 °C, and the development of an advanced numerical model based on the components' specifications. In this temperature range there are very few detailed studies up-to-date. The proposed HTHP was tested experimentally in 50 different working points selected based on the compressor's limits and on the general requirements for industrial applications requiring heat at high temperatures, up to 150 °C. The results show that the proposed HTHP can deliver a total heat of 38.6 kW at 148.5 °C, within a temperature lift of 66.8 K, with an electric power consumption of 10.7 kW, and with a heating coefficient of performance (COP) of 3.6. Moreover, using the external subcooler resulted in a substantial increase in the COP, which can reach 33 % compared with similar HTHPs without a subcooler. After successfully validating the HTHP model with the experimental results, extended performance maps were developed based on more than 500 possible operating conditions covering the most common steam generation and energy storage applications. Finally, four performance correlations were obtained, with an accuracy of ±10 %, hereby providing a black-box model to ease the integration of such HTHPs into dynamic simulations of industrial processes.

1. Introduction

In recent years, high-temperature heat pumps (HTHPs) have attracted increasing interest. The term HTHP is generally used in connection with industrial heat pumps, and often refers to heat pumps with heat sink temperatures above 100 °C. The system follows a vapor-compression cycle. The HTHP transfers heat from a lower-temperature heat source to a higher-temperature heat sink by means of a thermodynamic input in the form of either work of heat. The operation is similar to conventional heat pumps but with different refrigerants than in space and water heating applications. Additionally, the higher temperature and pressure in the cycle result in more demanding requirements for the cycle's components. A special attention is required in the compressor regarding the discharge temperature and the lubrication oil when working in high-temperature cycles. Consequently, careful, tailored designs and proper thermal management are required.

The increasing commitment to fight against climate change has pushed the research and market development of HTHPs, since they promote waste heat recovery and can become key technologies for the decarbonization of the industry. HTHPs could substitute, partially or totally, the use of fossil fuel boilers to produce pressurized hot water or steam in the industry.

Currently, heat pumps in the industrial sector deliver heat mainly up to 100 °C [1]. HTHPs, with higher delivery temperatures, are scarcely available on the market and are currently in the research phase, mainly in the form of lab-scale prototypes and with only a few industrial demonstrators [2]. According to Hamid et al. [3], heat pumps with delivery temperatures of 100 °C are already well-established in the industry, and the next target in HTHP technology is to reach from 100 °C

* Corresponding author.
E-mail address: miguel.ramirez@tno.nl (M. Ramirez).

https://doi.org/10.1016/j.applthermaleng.2024.122961
Received 17 November 2023; Received in revised form 22 February 2024; Accepted 13 March 2024
Available online 18 March 2024

Nomenclature

A	area [m^2]
COP	heating coefficient of performance [–]
D_h	hydraulic diameter [m]
DSH	desuperheating [K], or [°C]
f	friction coefficient [–]
G	mass flux [$kg/m^2 \cdot s$]
g	gravitational acceleration [m/s^2]
h	specific enthalpy [kJ/kg]
k	thermal conductivity [kW/m·K]
$\dot{m}$	mass flow rate [kg/s]
n_{comp}	compressor's speed [rps], or [1/s]
N_{exp}	number of experimental points [–]
p	pressure [MPa]
P_{el}	electrical power [kW]
Pr	pressure ratio [–]
$\dot{Q}$	heat transfer rate/capacity [kW]
$\dot{q}$	heat flux [kW/m^2]
s	entropy [kJ/kg·K]
SC	subcooling [K], or [°C]
T	temperature [°C]
t	wall thickness [m]
u	velocity [m/s]
V_{disp}	compressor's total displacement [m^3]
z	spatial position (flow direction) [m]
α	heat transfer coefficient [$kW/m^2.K$]
β	perimeter [m]
ΔT	temperature difference [K], or [°C]
$\dot{x}$	vapor quality [–]
η_{is}	isentropic efficiency [–]
η_{o}	overall compressor efficiency [–]
η_{v}	volumetric efficiency [–]
v	specific volume [m^3/kg]
∇	vector differential operator [–]
ρ	density [kg/m^3]
Φ	void fraction [–]
θ	inclination angle [deg.]
Ψ^2	two-phase multiplier for frictional pressure drop [–]

Subscripts

comp	compressor
cond	condensation/condenser
dis	discharge
evap	evaporation/evaporator
f	fluid
g	gas
HTHP	high-temperature heat pump
i	fluid cell index
in	inlet
is	isentropic
j	wall cell index
lift	temperature lift
loss	losses
max	maximum
melt	melting
min	minimum
out	outlet
PCM	Phase-Change Material
r	refrigerant
snk	sink
src	source
subc	subcooler
suc	suction or suction line
w	water
wall	plate wall

to 200 °C, where an estimated 27 % of industrial process heat demand is required. Further development and penetration of HTHPs in the industry require facing several challenges: technological (limitation of power consumption due to intensive electrification of the heating sector), economic (high investment and installation cost), regulatory, policy, and public acceptance issues. The technological challenge associated with intensive electrification of the heating sector is coupled with regulatory and policy considerations. However, the growing environmental awareness and the proliferation of both public and private decarbonization initiatives can help in this transition.

HTHPs have gained more and more attention in the last years: according to the latest report from the IEA Annex 68 on HTHPs [4], 34 technologies from different manufacturers are nowadays available. Although some of them have only been tested in the laboratory, 24 out of these 34 technologies have already been totally tested and qualified. The same report presented 18 demonstration cases in the industry. The heat sink was, in one case, hot water production; in 2 cases, a distillation process; in 4 cases, a drying process; and in 11 cases, steam production. Only 6 of these demonstrators employed closed-cycle vapor-compression technologies. The remaining 12 demonstrators employed either mechanical vapor recompression (9 cases) or thermally driven heat pumps (3 cases). The demonstration technologies have been installed in the refinery (4 cases); in the food and beverage industries (3 cases); in the pharmaceutical, sewage, and electronic industries (2 cases in each sector); and in the plastics, paper, and mineral industries (1 case in each sector).

Several studies, such as from Jung et al. [5], Wolf et al. [6], Kosmadakis et al. [7], and Marina et al. [8], show the potential of HTHPs for the decarbonization of numerous industrial processes in Europe and worldwide. The analyses reveal that the most relevant application areas for HTHPs are the food/beverage, chemicals, and pulp/paper industries for processes like drying, pasteurization, distillation, evaporation, sterilization, or similar thermal processes with available waste heat from about 30 °C to 70 °C, for process heat demand from 80 °C to 150 °C [9]. Although the number of HTHP demonstrators is still small, the large potential for its deployment is recognized by the IEA Net Zero report [10], which presents a detailed roadmap to achieve industrial processes with zero CO_2 emissions by 2050. The report presents a net zero scenario for 2050 in which around one-third of the total heat demand in the low ($T < 100$ °C) and medium (100 °C $< T <$ 400 °C) temperature range in the light industries is covered by heat pumps.

Additionally, HTHPs can be integrated into power-to-heat-to-power (P2H2P) systems that have gained more attention recently as a solution to mitigate the intermittency of renewable energy sources (RES). For example, the EU-funded "CHESTER" project [11] develops such a P2H2P solution, an innovative compressed heat energy storage (CHEST) system, which can efficiently store and manage thermal and electrical energy flows coupling supply and demand sides. The prototype presented in this work has been designed and tested considering the CHEST system application.

1.1. State of the ART in high-temperature heat pumps

In a recent review of industrial HTHPs, Jiang et al. [2] identified 15 experimental studies with prototypes operating at sink temperatures exceeding 130 °C. Among these studies, only three of them included measurements with sink temperatures above 140 °C, and just two of them reported sink temperatures above 150 °C. Table 1 summarizes the

Table 1
List of experimental works published found in the literature classified according to refrigerant used, compressor type, and maximum sink temperature.

Refrigerant name [Type]	Compressor type	T_{src} [°C]	$T_{snk,max}$ [°C]	COP [–]	Year/ Ref.
R-1336mzz(Z) [HFOs]	Scroll	83–117	>150	2.0–4.5	2023/ [14]
	Piston	50–110	>150	2.4	2015/ [15]
		45–95	>150	2.6–5.8	2016/ [16]
		30–80	140–150	1.8–4.3	2019/ [17]
R-1233zd(E) [HFOs]	Piston	30–80	140–150	2.1–4.7	2019/ [17]
R-1223yd(Z) [HFOs]	Piston	30–80	140–150	1.4–4.5	2019/ [17]
R-1234ze(E) [HFOs]	Piston	82	140–150 (air)	2–3.72	2019/ [18]
BY-5 [binary near-azeotropic mixture]	Scroll	70–80	130–140	2.2–3.1	2017/ [19]
NBY-1 [binary synthetic mixture]	Scroll	60–80	130–140	2.4–4.9	2019/ [20]
HT125 [synthetic mixture]	Piston	45–105	130–140	1.7	2016/ [21]
LG6 [synthetic mixture]	Piston	40–90	130–140	2.74	2015/ [22]
ECO3 [synthetic mixture]	Scroll	35–60	130–140	2–3	2012/ [23]
R-600 [Natural]	Piston	35–75	>150	2.7–4.5	2022/ [24]
R-601 [Natural]	Screw	40–90	130–140	3.0	1985/ [25]
Water [Natural]	Twin screw	70–85	140–150	1.9–6.1	2020/ [26]
	Centrifugal	90	130–140	5.5	2014/ [27]
NH_3 [Natural]	Twin screw	80–85	130–140	2.8–3.5	2016/ [28]
NH_3-H_2O [Natural mixture]	Hybrid compression-absorption (piston)	80–170 (flue gas)	>150	5.29	2022/ [13]
		ND	130–140	ND	2016/ [29]
R-245fa + Water [HFC + Natural mixture]	Piston(two stage)	60	130–140	3.5	2017/ [30]
R245 + BY3A R245 + BY3B BY6 + BY3A [Different refrigerant mixtures]	Piston	52–58	>150	2.3–3.2	2019/ [31]

type of compressor, the refrigerant, the heat source range and maximum heat sink temperature, and the range of COP values obtained in each of these studies. Another recent review by Adamson et al. [12] classified HTHPs according to their thermodynamic cycle. 49 cycle configurations were identified, out of which 12 have undergone experimental investigations. Two out of these 12 studies have been incorporated in Table 1; the remaining 10 have either been already included by Jiang et al. [2] or do not include a complete set of experimental data. Table 1 also covers two experimental studies that have been published since the previous reviews: one experimental study on the operation of a hybrid absorption-compression HTHP using NH_3/H_2O as refrigerant [13], and another work presenting experimental results of a HTHP with a scroll compressor using R-1336mzz(Z) as refrigerant [14].

Table 1 provides a summary of the experimental research conducted in the field, encompassing a total of 17 studies. Most of these studies, specifically 12 out of 17, focus on evaluating the performance of HTHPs using synthetic refrigerants. Within this category, six studies employ innovative ad-hoc refrigerant blends. Additionally, four studies investigate HTHPs employing fourth generation Hydrofluoroolefins (HFOs) refrigerants such as R-1223yd(Z), R-1233zd(E), R-1234ze(E) (transcritical cycle) or R1336mzz(Z). Two of the aforementioned studies present experimental results involving R-245fa in a cascade configuration with water or a custom refrigerant blend. In contrast, only five out of the seventeen studies explore the use of natural refrigerants, which include R-600, Pentane, NH3 (Ammonia), NH3/H2O, or water as their primary refrigeration medium.

The experimental studies with HTHPs utilizing HFOs are summarized in the upper rows of Table 1. To the authors' knowledge before the present publication, only the research groups responsible for these studies have conducted and published measurement campaigns involving HFOs in this temperature range.

Hassan et al. [32] compared the performance of different synthetic and natural refrigerants which can be employed in HTHPs designed for compressed heat energy storage applications. Their analysis showed that among these refrigerants, R-1233zd(E) could be a potential candidate for HTHP applications given its favorable environmental and thermal properties; besides, the performance is similar to the most commonly used refrigerant in HTHP applications (R-245fa).

Arpagaus and Bertsch [17,33] presented an experimental comparison between low GWP refrigerants, R-1224yd(Z), R-1233zd(E), and R-1336mzz(Z), and the hydrofluorocarbon (HFC) refrigerant R-245fa. This prototype's performance has also been compared with the data reported in Helminger et al. [16] and Nilsson et al. [34] showing similar trends, with Carnot efficiency values ranging between 29 % and 41 %.

Although the piston compressor is one of the key technologies in industrial heat pumps, many compressor manufacturers still do not include it in their range of compressors targeting the HTHPs applications.

Despite the fact that HTHPs market has grown steadily in recent years, the use of piston compressor technology in HTHPs applications is still limited and not developed much by many compressor manufacturers [35,36]. On the one hand, manufacturers such as Oilon [37] and Combitherm [38] offer HTHPs driven by piston compressors to supply heat up to 120 °C, using conventional piston compressors available in the market. On the other hand, manufacturers such as Heaten [39] and SPH [40,41] offer HTHPs with piston compressors specially developed for high-temperature applications in the capacity range between 0.5 and 10 MW. The manufacturer SPH recently offered a HTHP that supplies either hot water at 165 °C or saturated steam up to ≈0.6 MPa(a). From the authors' point of view, there is insufficient experimental data published up-to-date regarding these newly developed HTHPs. This reinforces the need for detailed experimental analysis of HTHPs driven by piston compressors, using low-GWP refrigerants such as R-1233zd(E).

This study analyzes experimentally and numerically the performance of a novel HTHP configuration under operating conditions which have not been previously explored in literature. Although the current work focuses on a specific HTHP case, the design, methodology, numerical modeling, and performance correlations can be of interest for other applications which require heat at constant temperatures, such as drying, sterilization, distillation, or direct steam generation. As a matter of fact, the current HTHP prototype has been experimentally tested and numerically validated under a wide range of operating conditions covering most steam generation and thermal energy storage applications.

Based on the previous literature review, the novelties of the presented work can be summarized as follows:

- Presenting an innovative design that incorporates a condenser and an external subcooler to supply the heat in two forms: latent and sensible. This configuration also results in a better matching between the flow streams inside heat exchangers.

- Testing a new variable-speed piston-compressor, using R-1233zd(E) as refrigerant, explicitly designed for HTHP applications that can endure an internal temperature of up to 215 °C and a discharge temperature of up to 160 °C.
- Developing and validating a detailed numerical model of the proposed HTHP that considers the components' specifications, a detailed discretization of the heat exchangers and tubes, and real performance curves of the compressor.
- Generation of extended performance maps that cover 576 possible operating conditions of particular interest for applications of steam generation and sensible and latent thermal energy storage.
- Deriving correlations to estimate the key performance indicators of the HTHP with an accuracy of ± 10 %. These correlations can be employed as a black-box model to enable the simulation of this HTHP in other applications. Furthermore, the correlations can be easily modified to upscale the system.

2. System concept and possible applications

The applications which were considered when designing the HTHP were steam generation and thermal energy storage applications. The idea was to split the delivered heat into two parts, latent and sensible, as exchanged in the condenser and the subcooler, respectively. This unique configuration allows for a better matching between the secondary-fluid and the refrigerant temperature profiles within the heat exchangers, minimizing the pinch points and the irreversibilities associated with the heat transfer process.

Hassan et al. [42] investigated the ability of the proposed HTHP configuration, Fig. 1, to generate superheated steam using different natural refrigerants. The results were promising and showed that at a source temperature of 70 °C and condensation temperature of 120 °C; the current configuration could produce superheated steam at 150 °C from pressurized water at 60 °C. At these working conditions, the HTHP reaches coefficient of performance (COP) values of 3.83, 3.81, 3.74, 3.42, and 3.30 with Propanone, n-Pentane, 1-Pentene, n-Butane, and Butene, respectively. The outlet steam temperature was fixed at 150 °C to ensure that the refrigerant discharge temperature is always ≤ 160 °C for the compressor's safety. The results of the current HTHP configuration were compared with the commercial SGH165 steam generation system presented by Kaida et al. [43]. SGH165 is a hybrid system which comprises a HTHP to produce saturated steam at 120 °C and a mechanical steam compressor to compress the steam up to 175 °C and 0.8 MPa(g). The refrigerant is a mixture between R-134a and R-245fa. To produce superheated steam at 150 °C recovering heat at 70 °C, the SGH165 yields a COP of ≈2.3 which is around 40 % lower than with n-Pentane in the proposed HTHP. The main reason for this is the high power consumption of the steam compressor that can reach 50 % of the total electrical consumption of the system. Using a subcooler in the presented HTHP configuration also gives an advantage for preheating the liquid water before the condenser, hereby opening the possibility to employ waste condensed water from any industrial process.

The option of integrating the proposed HTHP into a CHEST system was also investigated by Hassan et al. [44]. As illustrated in Fig. 2 (up), the HTHP charges a high-temperature thermal energy storage (HT-TES) system, where the latent heat is stored in a Phase-Change Material (PCM) that has a melting temperature of 133 °C, while the sensible heat is stored in a pressurized water tank. The source-side ranges between 40 and 90 °C and could be obtained with industrial waste heat or with a seasonal pit thermal energy storage (SP-TES) system. The electricity required for the compressor could be obtained from renewable energy sources (RES).

The Engineering Equation Solver (EES) program [45] was employed to develop a thermodynamic model of the current HTHP configuration integrated into the CHEST system using R-1233zd(E) as working fluid. The model helped to investigate the HTHP's working limits and components capacities. The main assumptions are: The CHEST system always works under steady state conditions; no heat losses in the HT-TES system; the PCM always melts and solidifies homogeneously at constant temperature; the heat stored by the HTHP is consumed by the organic Rankine cycle (ORC) with the same ratio; the refrigerant always enters the subcooler as saturated liquid; the refrigerant-side pressure drops in tubes and heat exchangers are neglected. The prosed EES model was validated successfully with the results of Jockenhöfer et al. [46].

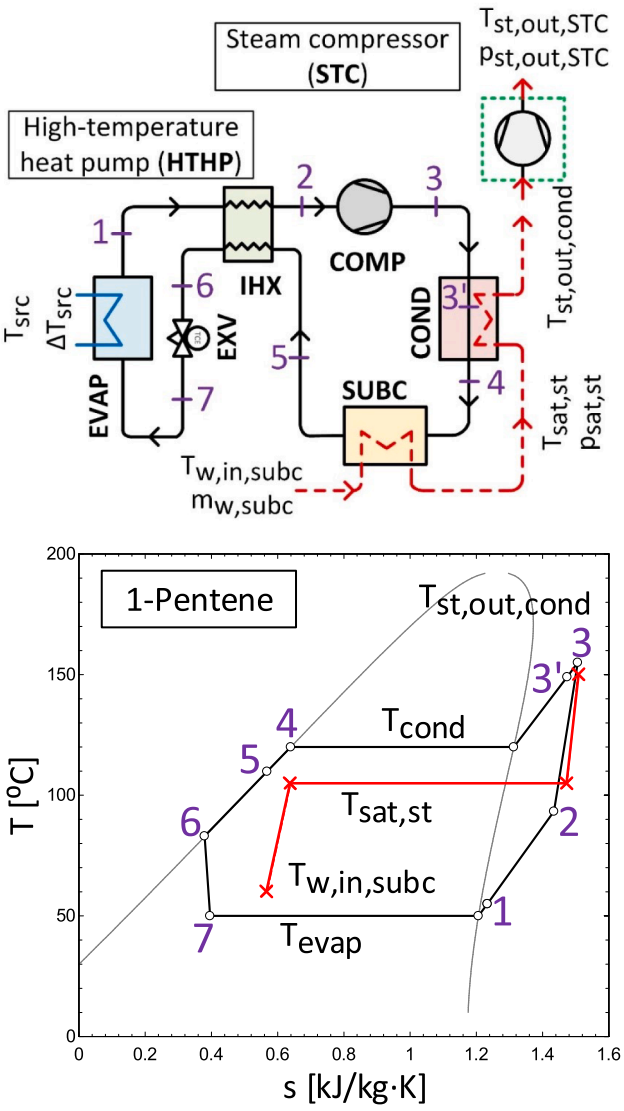

Fig. 1. (up) Proposed steam generation system (HTHP with/without steam compressor), (down) T-s diagram of the proposed HTHP using 1-Pentene.

Fig. 2 (down) shows an example of the numerical results of the current HTHP working between source and sink temperatures of 90 and 133 °C, respectively. The fixed parameters are: overall compressor efficiency $\eta_o = 60$ %; volumetric efficiency $\eta_v = 70$ %; compressor speed $n_{comp} = 25$ rps; evaporator's water-side temperature lift = 5 K; and pinch point in heat exchangers = 5 K. Under these working conditions, the proposed HTHP is capable of delivering a total heat of 62.5 kW by consuming 11.23 kW of electrical power, with a COP of 5.6.

Hassan et al. [32] discussed the main limitations and challenges of integrating the current HTHP into the CHEST system. They stated that the minimum source temperature should be ≈60 °C, instead of 40 °C, to avoid the high-temperature lift and high discharge temperature >160 °C. Another challenging factor is the heat loss, which can reach up to 45 % in such compressors. Controlling the compressor cooling process is crucial since high heat losses could result in liquid condensation at the

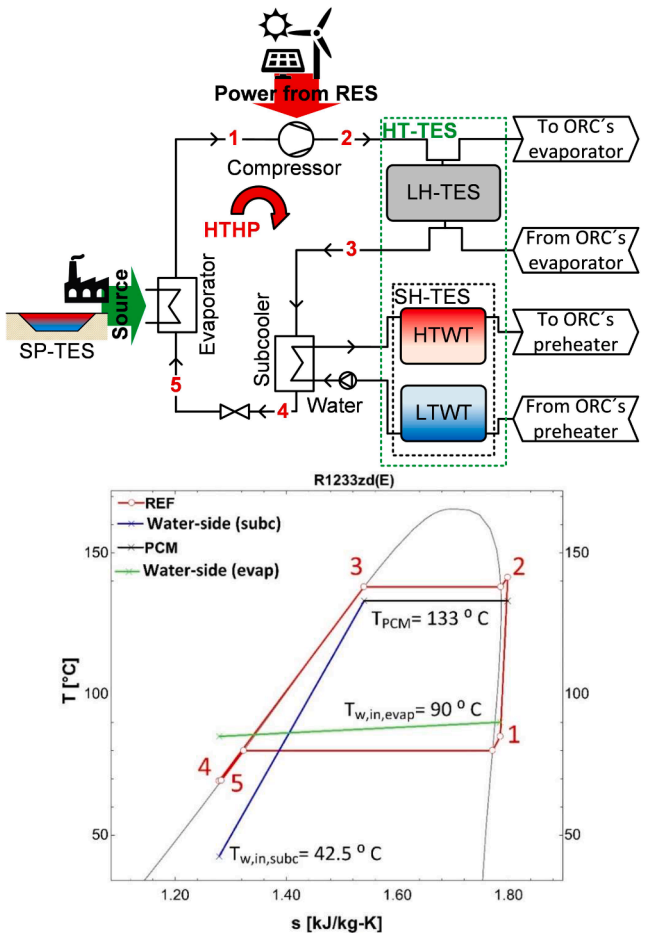

Fig. 2. (up) Conceptional integration of the current HTHP into the CHEST system, (down) T-s diagram of charging the CHEST system from 90 to 133 °C.

outlet of the compressor and in a low overall compressor efficiency. Another important aspect is the inlet water temperature range to the subcooler. The lower the inlet temperature to the subcooler, the higher the HTHP's performance. However, in this case, the main limitation is the water mass flow rate through the subcooler, which could fall below 150 kg/h (0.042 kg/s) and could cause control and stability problems. The partial load behavior of the HTHP is another challenge. This depends mainly on the available source heat, available electricity from RES, and state of charge of the HT-TES system. Based on the compressor's manufacturer, the compressor should run between 8.3 and 25 rps. However, the authors expected that the compressor could face some difficulties running stable at speeds <13.3 rps due to high vibrations and control issues.

3. Experimental setup and methods

3.1. Description of the laboratory setup

The HTHP prototype consists of a water-to-water vapor-compression refrigeration cycle. The configuration consists of a single-stage refrigeration cycle whose main components are the compressor, evaporator, condenser, subcooler, and the expansion device. Heat transfer to and from the HTHP is achieved using closed water loops. There are four separate pressurized water loops capable of delivering heating and cooling to the evaporator, the condenser, the subcooler, and the compressor's crankcase. All the heat generated by the HTHP is recycled by the thermal management system of the lab and delivered back to the HTHP to minimize energy consumption.

The prototype and the water loops are equipped with instrumentation to monitor the operating conditions. In addition, the prototype's pipelines and components, except the compressor casing, are fully insulated to avoid heat losses.

3.2. Main components

The HTHP uses a single-piston reciprocating compressor designed for high-temperature operating conditions. This is achieved owing to the sealing between the discharge side in the compression chamber and the lubrication system. This compressor has been experimentally tested in different HTHP prototypes using R-1336mzz(Z), achieving up to 150 °C as a heat sink temperature [34].

The condenser, evaporator, and subcooler are commercially available brazed plate heat exchangers (BPHXs) used for refrigeration applications. This choice is based on the low-capacity requirements, compact design, safety and performance. In addition, the plates type of design and their long thermal length improves heat transfer of two-phase flows. The expansion device is an electronic type which is controlled by an input signal. This allows flexibility in terms of configuration and can operate with any non-conventional working fluid. The control algorithm was designed by the authors in order to cover the requirements of the refrigerant and the working conditions applied to the heat pump. Besides the main components, the heat pump is also equipped with a liquid receiver, suction accumulator, oil separator, filters/dryers, valves, and the rest of the required auxiliary/safety components. Fig. 3 shows photographs of the proposed HTHP and the scheme of the main and auxiliary components, with an indication of the positioning of measuring sensors and transducers.

All the details and sizes of the components used in the HTHP are listed in Table 2. Moreover, further information about the criteria used for selecting the different components and details of the compressor has been discussed by Hassan et al. [32].

3.3. Testing campaign and methodology

The performance and capabilities of the HTHP prototype have been investigated under a wide range of operating conditions listed in Table 3. This range was selected based on the compressor's limits regarding the speed, internal and discharge temperatures, and the characteristics of the lubrication oil.

All tests were performed under steady-state conditions in accordance with the permissible deviations listed in EN-14511:3 [47]. The current HTHP was operated for 30 min in steady-state before starting the data collection. The data collection was limited to 30 min using a sequence of one second per data logged. The tests are grouped into two sets based on operating conditions. In the first set of tests, the evaporator and subcooler conditions changed while the condensing temperature was fixed at 134 °C. In the second set, the inlet water temperature to the evaporator and subcooler was fixed at 80 and 60 °C, respectively, while the outlet water from the condenser ranged from 100 to 150 °C.

The rationale behind this grouping was, for the first set the intention was to analyze the HTHP's performance when integrated into a CHEST system, where the heat delivered by the condenser is used to charge a PCM tank with a melting temperature of 134 °C and thermal capacity delivered to the subcooler is limited. The second set of tests was selected to explore the HTHP performance at different sink conditions keeping evaporator and subcooler temperatures stable. The $T_{w,in,evap}$ was selected as the middle temperature of the testing campaign and the $T_{w,in,subc}$ due to better stability of the control in the water side at these conditions. Only 18.3 and 25 rps compressor speeds were considered for this set of tests.

3.3.1. Data reduction and equations

Due to the configuration of the HTHP, the total heating capacity $\dot{Q}_{snk}$

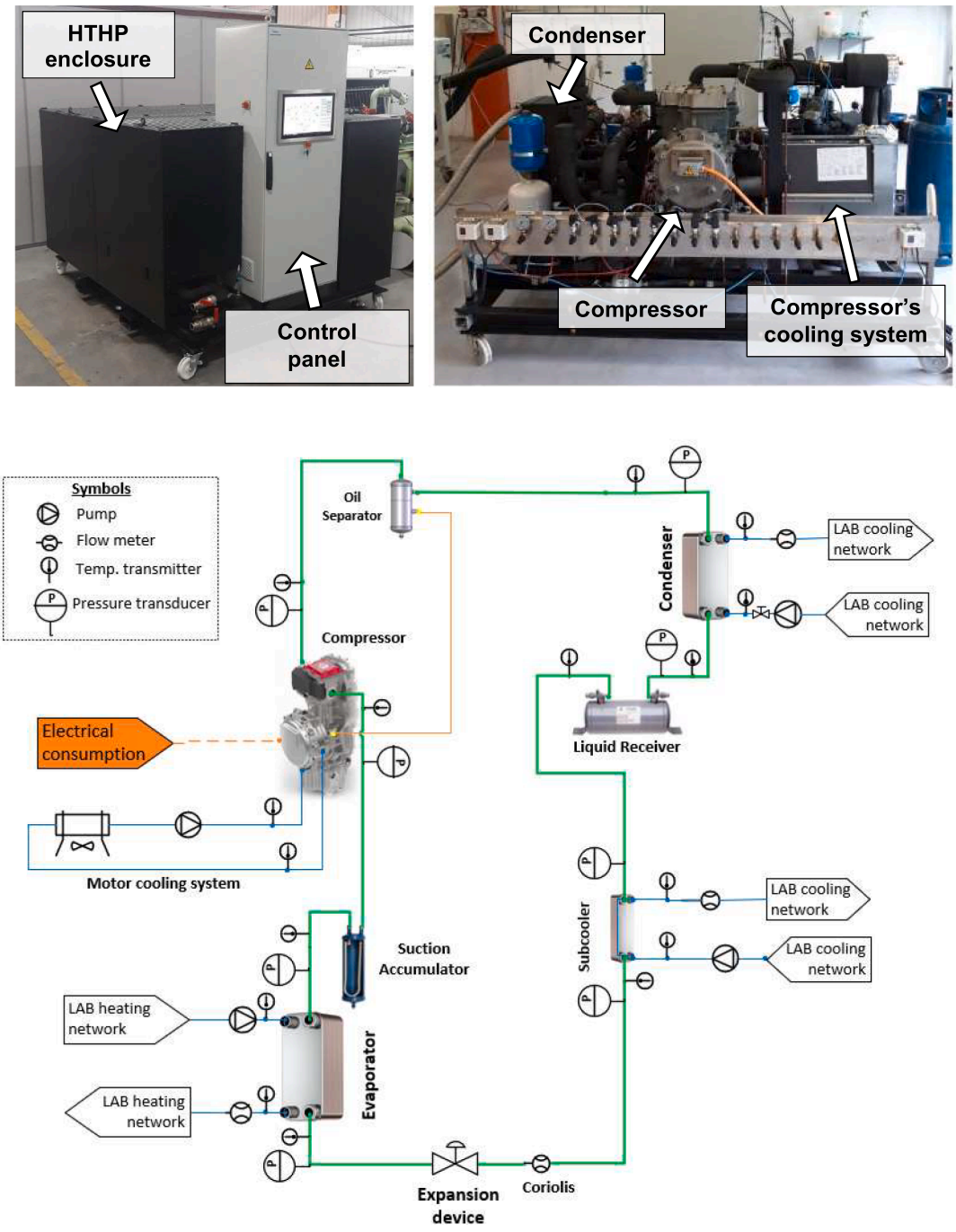

Fig. 3. Pictures (up), and scheme (down) of the HTHP.

is expressed as the sum of the condenser capacity ($\dot{Q}_{cond}$) and the subcooler capacity ($\dot{Q}_{subc}$). Eqs. (1)–(4) show the heat transfer rates for each heat exchanger based on the water side.

$$\dot{Q}_{cond} = \dot{m}_{w,cond} c_{p,w} \Delta T_{w,cond} \quad (1)$$

$$\dot{Q}_{subc} = \dot{m}_{w,subc} c_{p,w} \Delta T_{w,subc} \quad (2)$$

$$\dot{Q}_{snk} = \dot{Q}_{cond} + \dot{Q}_{subc} \quad (3)$$

$$\dot{Q}_{src} = \dot{Q}_{evap} = \dot{m}_{w,evap} c_{p,w} \Delta T_{w,evap} \quad (4)$$

The total heat losses to the ambient are estimated from the energy balance of the HTHP as seen in Eq. (5):

$$\dot{Q}_{loss} = \dot{Q}_{src} + P_{el,comp} - \dot{Q}_{snk} \quad (5)$$

The theoretical performance of the heat pump is calculated by Eq. (6):

$$COP_{Carnot} = \frac{(T_{cond} + 273.15)}{T_{cond} - T_{evap}} \quad (6)$$

The performance of HTHP is calculated by the heating COP, which is the ratio between the total heating capacity $\dot{Q}_{snk}$ and the power consumed by the compressor $P_{el,comp}$ (since the circulation pumps' consumption is negligible compared with the compressor's consumption), as shown in Eq. (7):

Table 2
List of the components of the HTHP prototype.

Component	Manufacturer/model	Specification	Value
Working fluid	Honeywell R-1233zd (E)	Charge	13 kg
Compressor	VHE HBC511	Displacement@24.2 rps	41.5 m^3/h
Condenser	SWEP B320	Heat transfer area	12.2 m^2
Subcooler	SWEP B86	Heat transfer area	2.88 m^2
Evaporator	SWEP V200	Heat transfer area	8.77 m^2
Expansion device	SIEMENS MVL661	Max. capacity	96 kW
Liquid receiver	CARLY RLHCY	Internal volume	40 l
Suction accumulator	CARLY LCY 1011	Internal volume	8.7 l
Oil separator	*CARLY Turboil 3009*	*Internal volume*	*2.5 l*

Table 3
Setting values of the water temperatures and the compressor speed for all the experimental campaign.

Tests	Evaporator Inlet	Subcooler Inlet	Condenser Outlet	Compressor speed
	[°C]	[°C]	[°C]	[rps]
1st set	70 80 90	40, 55, 70	134	13.3, 18.3, 25
2nd set	80	60	100–126	18.3
	80	60	100–150	25

$$COP = \frac{\dot{Q}_{snk}}{P_{el,comp}} \tag{7}$$

Regarding the compressor, there are three main parameters to evaluate its performance. The first parameter is the isentropic efficiency, which indicates how far the compression process is from the ideal one, as expressed in Eq. (8):

$$\eta_{is} = \frac{h_{dis,is} - h_{suc}}{h_{dis} - h_{suc}} \tag{8}$$

The enthalpy values at the suction (h_{suc}) and discharge (h_{dis}) are calculated using REFPROP V10 [48] using as input values the temperature and pressure at the mentioned points.

The second parameter is the volumetric efficiency, which expresses the volumetric flow rate referred to the theoretical value, as indicated in Eq. (9). The refrigerant mass flow rate ($\dot{m}_r$) is a measured value, and the volume at the suction (v_{suc}) line is calculated by REFPROP V10 using as input values the temperature and pressure at the compressor's suction. The theoretical volumetric displacement is evaluated by the internal volume of the cylinder and the corresponding compressor speed in rps.

$$\eta_v = \frac{\dot{m}_r \; v_{suc}}{V_{disp} \; n_{comp}} \tag{9}$$

The final parameter is the overall efficiency which relates the ideal, or isentropic, work to the electrical power consumption, as expressed in Eq. (10).

$$\eta_o = \frac{\dot{m}_r \left(h_{dis,is} - h_{suc}\right)}{P_{el,comp}} \tag{10}$$

The temperature lift of the heat pump is considered the difference between the outlet water temperature from the condenser and the water temperature entering the evaporator, as seen in Eq. (11).

$$\Delta T_{lift} = T_{w,out,cond} - T_{w,in,evap} \tag{11}$$

3.3.2. Monitoring and uncertainties

The sampling periods for all testing points have been selected under steady-state operation. The water temperature inlet conditions in the evaporator, condenser and subcooler are the main setpoint parameters. The frequency of measurements is one second, and the minimum sampling period is 20 min.

The refrigerant and the water loops are monitored with calibrated instrumentation responsible for reading temperature, pressure, flow rate, density, speed, and power consumption values. Temperature and pressure are measured at the inlet and outlet of the heat exchangers, expansion valve, and compressor. The mass flow rate and density are measured in the liquid line before the expansion device. The prototype is equipped with a control and power supply cabinet, with instrumentation for measuring the power consumption. The thermodynamic properties of the refrigerant are calculated using REFPROP V10. In addition, the water flow rate and temperature are measured at the inlet and outlet of the heat exchangers and the compressor's oil cooling loop.

The measured parameters, the specifications of data acquisition equipment, and their accuracy values are listed in Table 4.

The uncertainties have been calculated using the error propagation method [49]. The total uncertainties include three components: the test uncertainty (based on the standard deviation), the resolution uncertainty, and the precision uncertainty. A normal distribution is assumed for the test and precision uncertainties, while a triangular distribution is assumed for resolution uncertainty.

4. Experimental results

A total of 50 tests were performed during the experimental campaign, accounting for a total operating time of 67 h. The testing periods varied between 20 and 80 min and data was collected during steady-state condition.

4.1. HTHP performance

As mentioned before, the heating and cooling capacity values have been calculated from the measurements of the water side. The total heating capacity ($\dot{Q}_{snk}$) is the sum of the heat delivered by the condenser ($\dot{Q}_{cond}$) and the subcooler ($\dot{Q}_{subc}$) to their respective water loops. The source capacity is the heat transferred to the evaporator by the water loop ($\dot{Q}_{src}$). The water temperatures set for the evaporator, subcooler, and condenser are presented in Table 3.

The resulting $\dot{Q}_{snk}$ of the HTHP ranged between 15.5 and 66.1 kW, while the $\dot{Q}_{src}$ was between 16.1 and 56.6 kW during the first set of tests. In the same set of tests, the HTHP was tested under three different subcooler inlet water temperature values ($T_{w,in,subc}$), for every heat source temperature maintaining a fixed condensing temperature of 134 °C. For a given compressor speed, the HTHP performed better under $T_{w,in,subc}$ = 40 °C, as seen in Fig. 4; the lower the $T_{w,in,subc}$, the higher the $\dot{Q}_{snk}$. The lower the $T_{w,in,subc}$, the higher the temperature difference of both flows in the heat exchanger, as also observed by Hassan et al. [32]. This results in a higher heating capacity in the subcooler and therefore in the overall heating capacity, while the compressor's work remains equal. For a given $T_{w,in,subc}$, increasing the compressor speed, also increases the heat delivered by the HTHP as expected. The $\dot{Q}_{snk}$ under compressor speeds of 25 rps was by 26–29 % higher than for 18.3 rps, under all $T_{w,in,subc}$. While for 13.3 rps the $\dot{Q}_{snk}$ was by 23–33 % lower than under 18.3 rps for all all $T_{w,in,subc}$ values too. However, by increasing the compressor speed, the refrigerant mass flow rate increases, as well as the pressure drop and, therefore, the compressor consumption. For the same operating temperatures, the $\dot{Q}_{snk}$ of the HTHP increased by 27 % when increasing the compressor speed from 18.3 rps to 25 rps, while the $P_{el,comp}$ increased by 32 %, resulting in a drop of COP of 7 %. This was also observed in the numerical analysis of Hassan et al. [28].

$\dot{Q}_{subc}$ and $\dot{Q}_{cond}$ were approximately in the same range. The heat

Table 4
Specifications of the measuring equipment and their accuracy and uncertainties for measured and calculated variables.

Parameter	Sensor type/model	Range	Accuracy	Uncertainty
Refrigerant temperature	PT-1000 AKS21	0–200 °C	±0.2 °C	0.2–2.6 °C
Water temperature	PT-100	0–160 °C	±0.1 °C	0.1–3.3 °C
Refrigerant pressure	Pressure transducer	0–3 MPa(g)	typical ± 1 % full scale, max ± 4 % full scale	0.014–0.06 MPa
Refrigerant flow rate	Coriolis SIEMENS Sitrans FC-430	0.2–1.2 kg/s	±0.1 %	0.001–0.012 kg/s
Water flow rate	Electromagnetic Siemens Sitrans FM- MAG 3100	0186 l/s	±0.2 %, ±0.37 l/s	0.37–1.45 l/s
Current	Beckhoff EL3403 power measurement terminal + 3 Carlo Gavazzi CTD-1X current transformers	050 A pro phase(full scale)	0.5 % to full scale	–
Voltage	Beckhoff EL3403 power measurement terminal	0–500 V pro phase(full scale)	0.5 % to full scale	–
Calculated Variables				
Compressor's electric power ($P_{el,comp}$)		4.1–14.1 kW	–	0.03–0.20 kW
Condenser's capacity ($\dot{Q}_{cond}$)		7.6 –43.5 kW	–	1.3–4.6 kW
Subcooler's capacity ($\dot{Q}_{subc}$)		5.4 –29.7 kW	–	0.2–0.9 kW
Evaporator/source capacity ($\dot{Q}_{src}$)		8.3–44.9 kW	–	1.4–4.5 kW
COP		3.6– 6.9	–	0.1–0.8

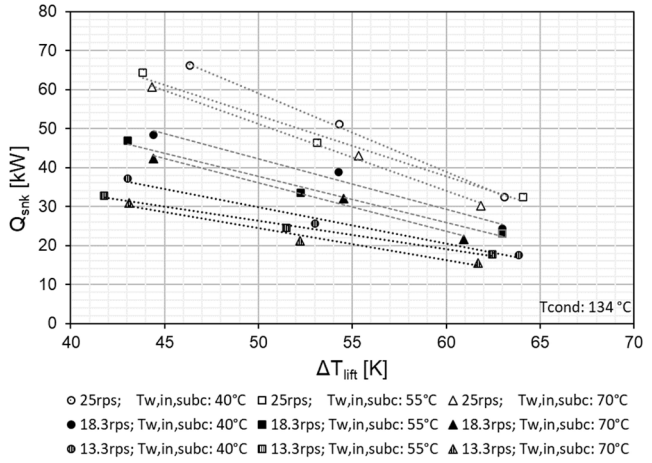

Fig. 4. Total heating capacity ($\dot{Q}_{snk}$) versus the temperature lift for stable condensation temperatures at different compressor speeds and subcooler's water inlet temperatures.

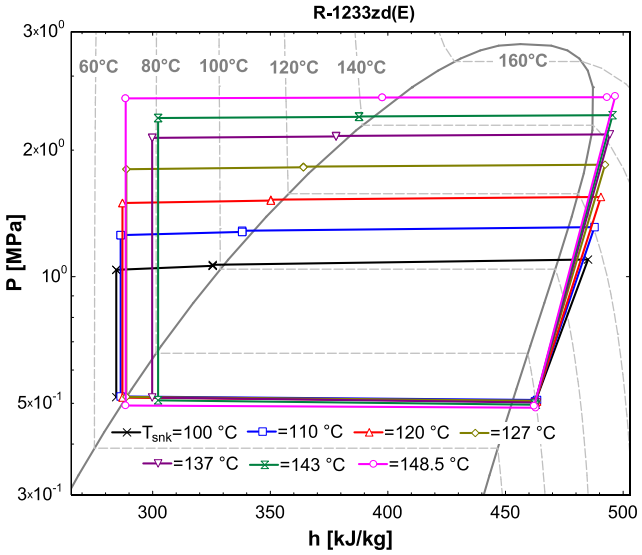

Fig. 5. p-h diagram of the proposed HTHP delivering heat at different sink temperatures under constant $T_{w,in,evap}$ = 80 °C, $T_{w,in,subc}$ = 60 °C, and n_{comp} = 25 rps.

delivered in sensible heat form, the subcooler delivered between 44.8 % and 52.2 % of the total heat provided by the heat pump, with the remaining heat coming from the condenser. The water temperature lift inside the subcooler $\Delta T_{w,subc}$ was measured between 32.5 and 104.7 K, achieved by maintaining a low mass flow between 0.02 and 0.11 kg/s. This HTHP is therefore applicable for processes where two loads must be covered, one for steam generation covered by $\dot{Q}_{cond}$, and the second for heating processes with high temperature lift requirements which can be supplied by $\dot{Q}_{subc}$. The waste heat required ($\dot{Q}_{src}$) must be higher than the individual sink sides.

The heat losses ranged between 2.2 and 7.3 kW, which in some cases exceeded the expected theoretical values by up to 10 %. The sources of heat losses were identified mainly through the enclosure of the compressor and a small part via the compressor's oil-cooling water loop. The corresponding fraction of each source on the total heat losses could not be accurately measured due to the lack of appropriate measuring devices at each source.

During the second set of tests, the heating capacity of the condenser decreased as the condensing temperature increased. At the same time, the heating capacity of the subcooler $\dot{Q}_{subc}$ was also enlarged. This derives from the slope of the saturation lines and the thermodynamic properties of the refrigerant. As observed in the P-h diagram of R-1233zd (E) (Fig. 5), the higher the condensing temperature, the lower the available latent heat.

For the cases of $T_{w,out,cond}$ = 137 °C and 143 °C the water flow rate within the subcooler was controlled automatically which caused the subcooling degree to drop. This resulted in lower evaporating and condensing capacities as shown in the P-h diagram in the cases of red and brown cycles.

Fig. 6 presents the COP tendency as a function of the temperature lift of the HTHP. The values represent the theoretical COP_{Carnot} and the COP values of the heat pump, including their respective error margins. The COP of the HTHP ranged between 3.3 and 7 for ΔT_{lift} values between 15 and 67 K. As expected, the results showed better COP under low-temperature lifts and low values of inlet water temperature to the subcooler.

The highest COP was recorded during the test with the lower temperature difference between the evaporator water inlet and the condenser water outlet. This case was the test point with a heat source temperature of 80 °C and a water inlet temperature to the subcooler of 60 °C. The water outlet temperature from the condenser was 96 °C for a compressor speed of 18.3 rps. However, these high COP values were observed at very low ΔT_{lift} values. These values were included in the testing campaign as extreme points and could be defined as unrealistic

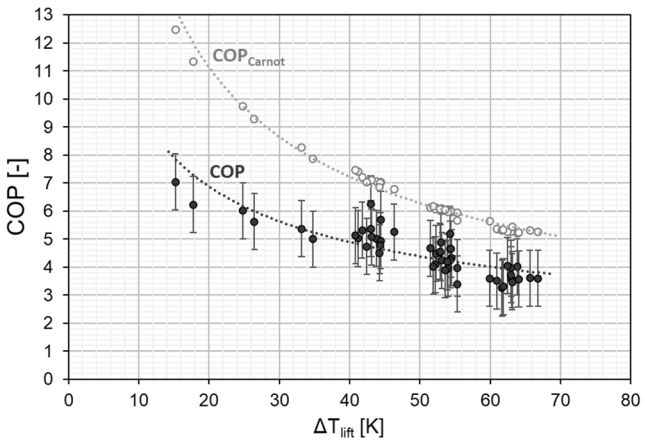

Fig. 6. COP_{Carnot} and COP values over the temperature lift range.

conditions to run a HTHP.

The resulting COP values from this study have been compared to the correlations found in the literature (Fig. 7) for experimental results of similar laboratory-scale HTHPs. These studies present experimental results of HTHPs using either R-1233zd(E) or R-1336mzz(Z) [50,16,34]. One of these correlations, that are presented in Arpagaus et al. [17,33,50] has been obtained from measurement of a heat pump designed with the same compressor from Viking Heat Engines used in our study, but that has been measured operating with R-1336mzz(Z) [34].

The HTHP is not equipped with an internal heat exchanger (IHX). The idea was to take maximum advantage of all the hot liquid refrigerant after the condenser to store the heat in a sensible form using the subcooler. In addition, both the condenser and the subcooler use different water loops which can be regulated individually. Therefore, the current COP values are comparable with those presented in Arpagaus et al. [1] in which the IHX is not included in the loop. It can be seen that for values of ΔT_{lift} above 60 K, the current COP values are similar to the mentioned study. In addition, the COP values for operation including the subcooler are up to 2 units higher than the studies considered in Fig. 7. The COP values are slightly wider spread due to the impact of the different subcooler water inlet temperatures on the subcooler's heating capacity. The improvement of the COP of this heat pump configuration is mainly due to the individual water loop cooling the subcooler at temperatures below 60 °C. This allows the rise of the sensible heat transfer rate, also increasing the temperature glide, and therefore, the overall thermal capacity of the system.

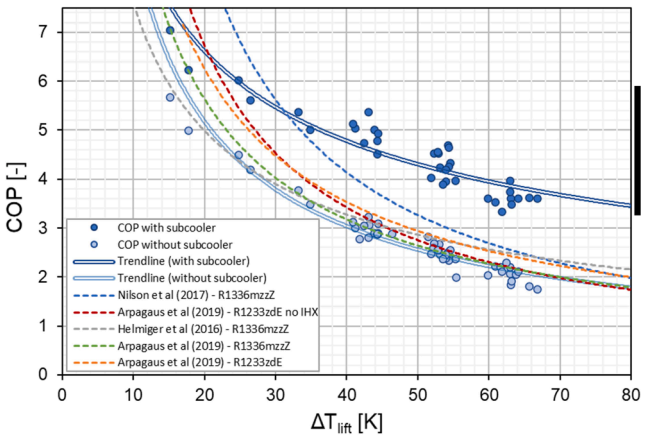

Fig. 7. Comparison of the COP trendlines of the HTHP experimental results (with and without the subcooler), with data from literature over the HTHP temperature lift.

4.2. Compressor performance

In the current study, the suction pressure ranged between 0.38 and 0.65 MPa(a) and the discharge pressure between 1.03 and 2.7 MPa(a). These operating conditions resulted in Pr values between 2 and 5.8 which correspond to ΔT_{lift} values from 15.2 to 66.8 K.

The measured suction and discharge temperatures versus the pressure ratio values are presented in Fig. 8. The suction temperatures ranged between 69 and 90 °C, while the discharge temperatures ranged between 108.7 and 154 °C, respectively. As expected, the higher the difference between the suction and discharge temperatures, the higher the pressure ratio. This leads to more work from the compressor, and to higher electric power consumption.

The power consumption of the compressor is presented in Fig. 9 versus pressure ratio values. The electric energy consumed by the compressor increases with the compressor speed as it is observed for the tests implemented under 13.3, 18.3 and 25 rps speed values. The lowest power consumption is 4.3 kW under a compressor speed of 13.3 rps, source temperature of 70 °C, and sink temperature of 135 °C. The maximum power consumption is 12.8 kW and was recorded during the test performed under 90 °C and 134 °C heat source and heat sink temperatures, respectively, at a compressor speed of 25 rps. For similar compressor speeds, the higher the pressure ratio, the lower the power consumption. This is a result of the density of the vapor in the suction line. The higher the Pr, the lower is the suction line temperature, which results in a lower density of the suction vapor and therefore less energy required by the compressor to compress the vapor.

The calculated volumetric efficiency η_v of the compressor varied between 57 % and 82 %, as shown in Fig. 10. As expected, the η_v is inversely proportional, in a linear relationship, with the pressure ratio as the internal losses increase with higher pressure ratio values. The η_v values under the speed of 25 rps are higher by 3–5 % than the ones under the speed of 18.3 rps.

The isentropic efficiency η_{is} was calculated using the temperature and pressure measurements at the suction and discharge of the compressor. The heat losses of the compressor are high (up to 18 % of the total heat delivered), hereby shifting the discharge temperature near to the saturation line, as seen in Fig. 5. This could result in η_{is} values $\geq$100 %. The η_{is} values presented in Fig. 10 are from the second set of tests under a compressor speed of 18.3 and 25 rps. η_{is} is higher for low compressor speeds since, for high-speed values, the heat losses and pressure drop within the valves are higher, which could have an impact on the sealing performance within the cylinder.

As mentioned previously, the oil cooling and the heat dissipated through the compressor casing were the primary sources of the heat losses. The latter were in the range of 2.2 –7.3 kW, corresponding to

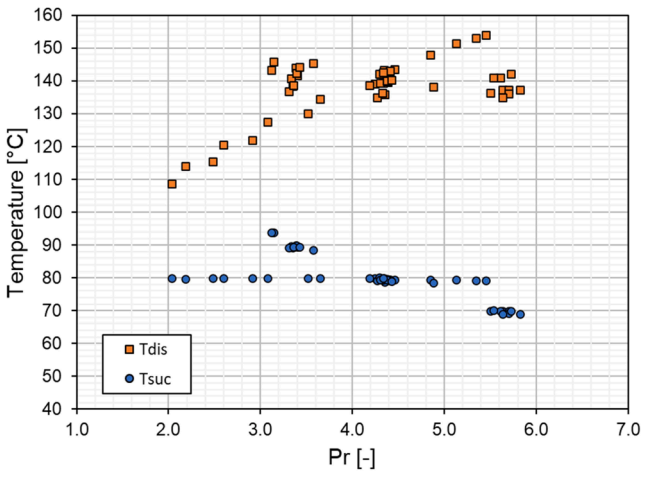

Fig. 8. Compressor's suction and discharge temperatures vs. the pressure ratio.

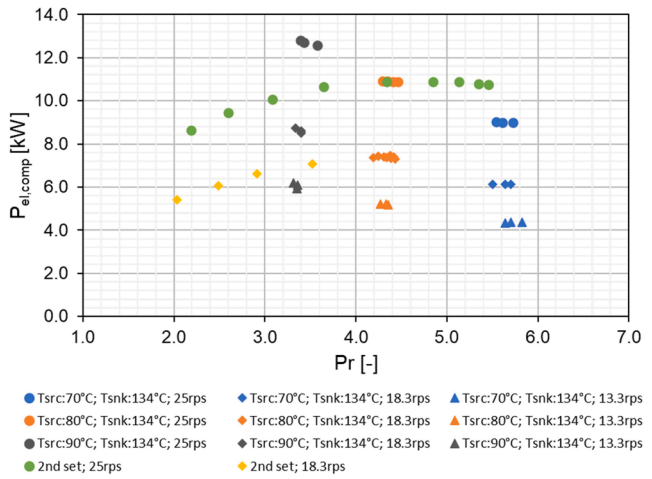

Fig. 9. Electrical power consumption of the compressor at different heat source and sink temperatures vs. the pressure ratio values.

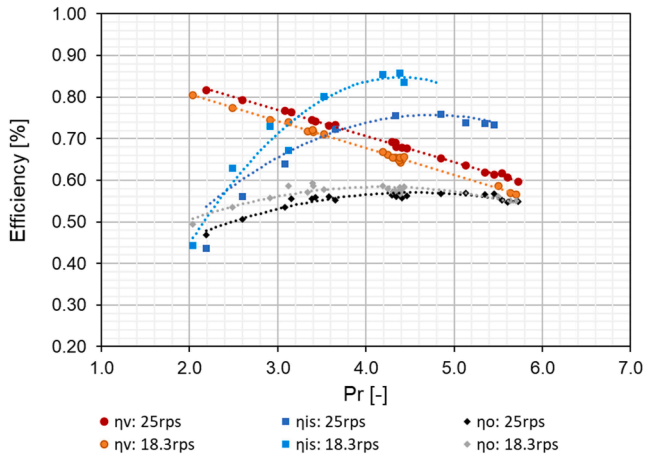

Fig. 10. Compressor's volumetric, isentropic, and overall efficiency values under compressor speeds of 18.3 and 25 rps over the pressure ratio values.

5–18 % of the total heating capacity of the HTHP. The compressor overall efficiency η_o presented higher values under 18.3 rps than for 25 rps, ranging from 47 to 62 %. The higher values were observed between Pr = 3 and 4.5.

The oil temperature in the crankcase was maintained at 90 °C by controlling externally the flow rate and the return temperature of the cooling water. The motor is enclosed in the compressor's case, which causes a temperature rise with the power consumption. In Fig. 11 the mean oil temperatures are presented over the compressor's power consumption. Considering the suction temperature values shown in Fig. 8, which are mainly at 80 °C, the oil temperature depends mainly on the power consumption and not on the suction temperature. This shows the importance of this specific compressor design where the suction gas is not in contact nor near from the motor, which is a common practice for conventional semi-hermetic reciprocating compressors to use the suction gas to cool down the electrical motor. Therefore, in the current compressor, the suction gas temperature can be increased above the operation limits of the electric motor.

Significant solubility values of refrigerant in oil were observed during the first tests. This was solved substantially by maintaining the oil temperature at approximately 5 K above the evaporation temperature, besides preheating externally the oil separator during the cold start-ups.

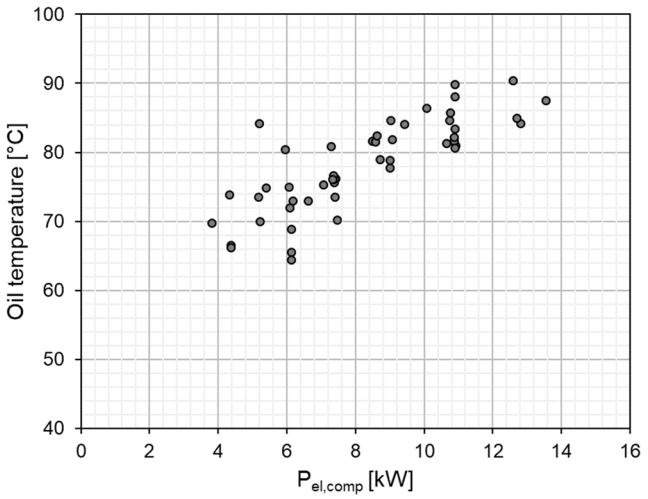

Fig. 11. Compressor's oil temperature values during operation versus the compressor power consumption.

5. Numerical modelling and performance map

5.1. HTHP model description

The current HTHP numerical model has been developed with the IMST-ART simulation tool [51]. IMST-ART combines accurate and fast algorithms and powerful analysis capabilities into a single software capable of simulating and analyzing the majority of vapor-compression refrigeration systems with almost any refrigerant and secondary fluids. IMST-ART can simulate a wide range of applications such as domestic freezers, supermarket cabinets, cold warehouses, air-conditioning units, heat pumps, mobile air-conditioning, and refrigeration equipment.

The solution methodology, reported by Hassan et al. [32], to solve the proposed HTHP cycle can be summarized as follows:

- Step 1: Input data:

The input data are introduced directly using the graphical interface of the "Working Cycle" feature shown in Fig. 12 a, by specifying:

- o Refrigerant: IMST-ART includes an extended thermo-physical library for most refrigerants used in conventional heat pumps; including special refrigerants for HTHP applications, for example, R-1233zd (E), R-1336mzz(Z), R-1234ze(Z), and Butene among others.
- o Condenser and Evaporator: heat exchanger type (IMST-ART accounts for finned-tube, brazed-plate, tube-and-wire, and microchannel heat exchangers, in the current case the BPHX is the selected one), secondary fluid data (type, inlet temperature, and outlet temperature or flow rate), and heat exchanger geometrical data (external dimensions, plate material, number of plates, plate pitch, plate thickness, area enhancement factors, and port diameter).
- o Compressor: catalog data (parametric tables for mass flow rate and electrical power consumption as a function of compressor speed, and saturation suction and discharge temperatures), compressor speed, total displacement, oil volume, oil circulation rate, and heat losses percentage.
- o Accessories: subcooler (single-phase BPHX), connection lines specifications (material, lengths, internal diameters, number of elbows, and type and thickness of insulation).
- o Heat pump working conditions: condenser outlet (fixed subcooling value, liquid receiver volume, or refrigerant charge), and expansion device type (fixed superheat value, capillary tube, or short tube with orifice).

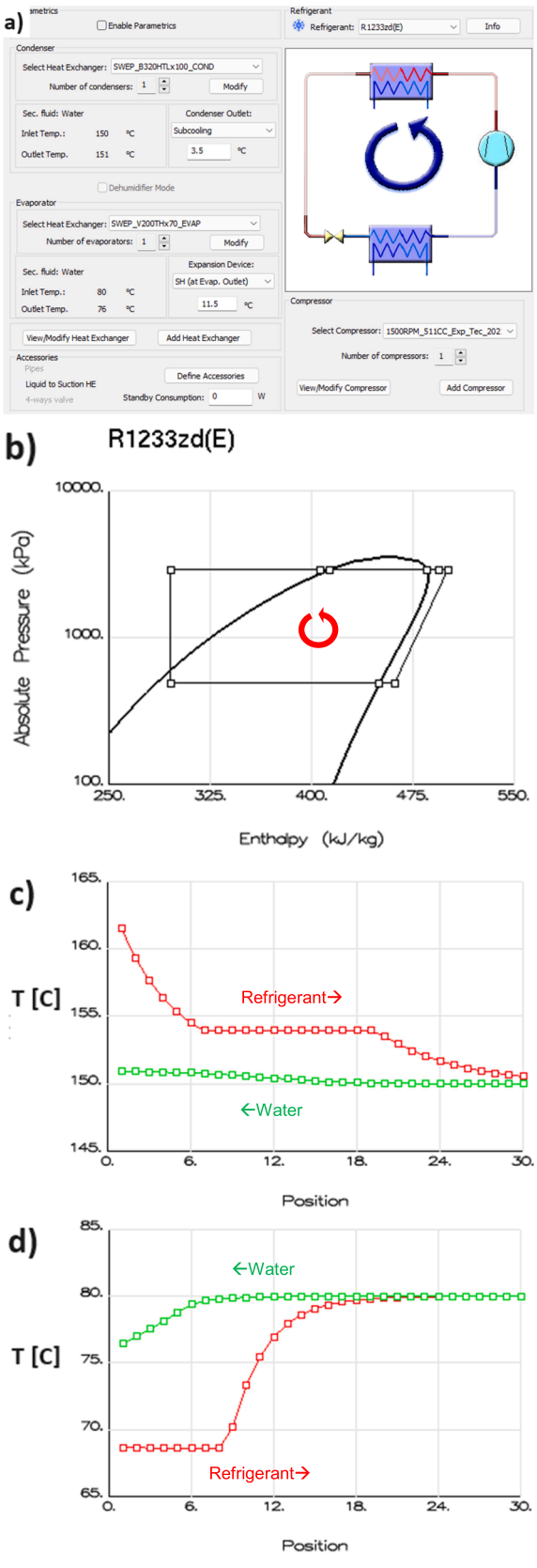

Fig. 12. (a) GUI of the "Working Cycle" feature in IMST-ART, (b) p-h diagram of the HTHP cycle under $T_{src} = 80°C$, $T_{snk} = 150°C$, and 25 rps, (c) temperature profiles inside the condenser, and (d) temperature profiles inside the evaporator.

The previous components can be saved as stand-alone files to be uploaded directly in any other HTHP cycle.

- Step 2: Discretization and initialization:
  - o Compressor: parametric tables are generated for the compressor's overall and volumetric efficiency based on input performance data. They are employed to estimate the electrical power consumption (Eq. (11))and refrigerant mass flow rate (Eq. (10)).
  - o Heat exchangers and tubes: they are discretized into segments along the refrigerant flow direction. The local variables for each segment are initialized. These include, for example, inlet and outlet velocities, flow rates, pressures, and temperatures.
- Step 3: Cycle's initial solution:
  - o The evaporation and condensation temperatures/pressures are estimated based on the secondary fluids' temperature lift.
  - o The compressor's sub-model is used to estimate the mass flow rate of refrigerant based on the estimated pressure ratio and suction enthalpy.
  - o Based on the previous estimations, heat exchanger's sub-model helps calculate the initial solution for the evaporator, condenser, and subcooler.
- Stage 4: Cycle's calculations and iteration process:
  - o Each HTHP's component has its own sub-model inside IMST-ART to estimate the outlet pressure and enthalpy based on the input pressure, enthalpy, and mass flow rate in the form: $f\left(p_{in}, h_{in}, p_{out}, h_{out}, \dot{m}\right) = 0$. Therefore, the problem is reduced to a system of non-linear equations which is solved iteratively, as mentioned by Corberan and Gonzalvez [52].
  - o This system of equations is solved using a standard solver which follows the MINPACK subroutine HYBRD1 [53]. The latter is based on a modification of Powell's hybrid algorithm. This algorithm is a variation of Newton's method, which uses a finite-difference approximation to the Jacobian and takes precautions to avoid large step sizes or increasing residuals. For a detailed description of the method, refer to Powell [54].
  - o The Euclidean norm, square root of the sum of squares, of this set of equations is used as the global convergence criteria. A valid solution is expected when the Euclidean norm $\leq 1x10^{-6}$ [52].
  - o The heat exchanger's sub-model is based on the semi-explicit method for the wall temperature linked equation (SEWTLE) proposed by Corberán et al. [55]. The solution procedure starts with the initial estimation of the wall temperature field. Based on this, the refrigerant and secondary fluids properties are estimated by applying mass (Eq.12), energy (Eq.13), and momentum (Eq.14) balances within each cell in the flow direction. The heat transfer coefficient and friction factor values are evaluated specifically in each segment based on the flow type and boundary conditions.

$$\rho u = G = constant \tag{12}$$

For single-phase flow:

$$GA\frac{d(h+u^2/2)}{dz} = \sum_{j=1}^{2}\beta_j\alpha_j\left(T_{wall,j} - T\right) \tag{13a}$$

For two-phase flow:

$$GA\frac{d}{dz}\left[x\left(h_g + \frac{G^2x^2}{2\rho_g^2\varphi^2}\right) + (1-x)\left(h_f + \frac{G^2(1-x)^2}{2\rho_f^2(1-\varphi)^2}\right)\right] + GA(gsin\theta) = \sum_{j=1}^{2}\beta_j\alpha_j\left(T_{wall,j} - T\right) \tag{13b}$$

For single-phase flow:

$$-\frac{dp}{dz}=f\frac{\rho u^2}{2D_h}+\frac{d(\rho u^2)}{dz}+\rho g sin\theta \tag{14a}$$

For two-phase flow:

$$-\frac{dp}{dz}=\frac{2fG^2(1-x)^2}{D_h\rho_f}\Psi^2+G^2\frac{d}{dz}\left[\frac{x^2}{\varphi\rho_g}+\frac{(1-x)^2}{(1-\varphi)\rho_f}\right]+\left[\varphi\rho_g+(1-\varphi)\rho_f\right]gsin\theta \tag{14b}$$

$$kt\left(\nabla^2 T_{wall}\right)=-\sum_{i=1}^{2}\dot{q}_i \tag{15}$$

Eq. (15) represents a balance between the longitudinal heat conduction between the current wall cell and the neighboring wall cells (left-hand side) and the heat transfer to/from the surrounding fluid cells (right-hand side). By integrating Eq. (15), the wall temperature field is updated based on the new estimation of the fluid temperature. The boundary conditions are given by the temperatures and pressures of the fluids at the entrance of the heat exchanger, and by the adiabatic condition for the outer plates of the heat exchanger. The previous steps are repeated inside an internal iteration loop until reaching convergence. The convergence is achieved when the residual of energy balance between the refrigerant- and secondary fluid-side is less than or equal to 1×10^{-6}.

- Step 5: Output data:

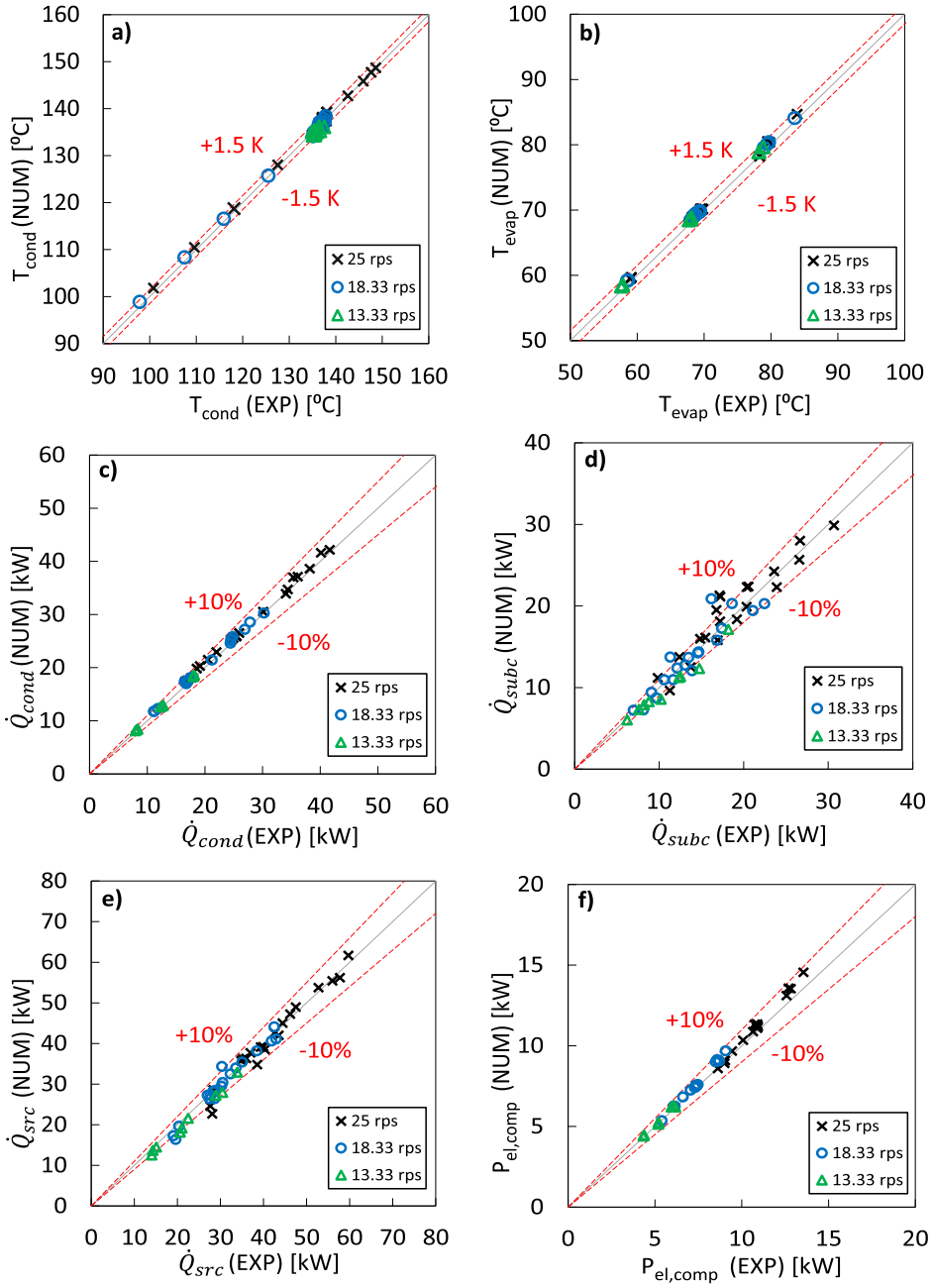

Fig. 13. Comparison of estimated numerical (NUM) and experimental (EXP) data of (a) T_{cond}, (b) T_{evap}, (c) $\dot{Q}_{cond}$, (d) $\dot{Q}_{subc}$, (e) $\dot{Q}_{src}$, and (f) $P_{el,comp}$ for n_{comp} = 25, 18.3, and 13.3 rps.

- o The cycle and components results are stored and shown to the user. To ease the detailed analysis of the results, IMST-ART also allows exporting all the results to an external Excel file or as a PDF report.
- o The results include, for example, the cycle representation on a p-h diagram (Fig. 12 b), detailed temperature profiles inside heat exchangers (Fig. 12 c and d), compressor's performance parameters, and overall performance indicators for the given operating point.

5.2. Model validation

The developed HTHP model was successfully validated against the 50 test points of the experimental campaign. The estimated values of evaporation and condensation temperatures are within ±1.5 K error bands with mean absolute error (MAE) values of ±0.58 K and ±0.60 K, respectively. The deviation of ±1.5 K was selected since the validation of the evaporation and condensation temperatures in literature usually ranges between ±1 and ±2 K. Predicting well these temperature limits is crucial for the estimation of the compressor work and mass flow rate. In the current study, the MAE for any parameter is calculated based on Eq. (16):

$$MAE\begin{cases} = \frac{1}{N_{exp}}\sum_{1}^{N_{exp}} |Predicted\ parameter - Measured\ parameter|, \ as\ a\ mean\ absolute\ difference \\ = \left(\frac{1}{N_{exp}}\sum_{1}^{N_{exp}} \left|\frac{Predicted\ parameter - Measured\ parameter}{Measured\ parameter}\right|\right) \times 100, \ as\ a\ mean\ absolute\ percentage \end{cases} \quad (16)$$

The MAE of condenser capacity ($\dot{Q}_{cond}$), subcooler capacity ($\dot{Q}_{subc}$), and source/evaporator capacity ($\dot{Q}_{src}$) are ± 2.82%, ±8.30 %, and ±4.36 %, respectively. Generally, the proposed HTHP model is capable to predict ≈87 % of the heat capacities within ± 0 % error bands, while the ≈13 % of values are within ±15 % error bands. The numerical values of the compressor's electrical power consumption ($P_{el,comp}$) are within ±10 % error bands with a MAE of ±2.76 %. Fig. 13 compares the numerical and experimental performance parameters under compressor speed values of 25, 18.3, and 13.3 rps.

5.3. Detailed HTHP's performance maps and correlations

Once validated, the numerical model was used to generate extensive performance maps for the proposed HTHP. These maps are based on five main independent variables, which are: the compressor speed n_{comp}, the inlet water temperature to the evaporator $T_{w,in,evap}$, the water temperature lift inside the evaporator $\Delta T_{w,evap}$, the inlet water temperature to the condenser $T_{w,in,cond}$, and the inlet water temperature to the subcooler $T_{w,in,subc}$. The water temperature lift inside the condenser $\Delta T_{w,cond}$ was fixed at 1 K to reproduce the PCM melting or the water evaporation inside the condenser. These variables are selected since they are they typically define the operational limits for any HTHP.

Table 5 shows the range of independent variables used to generate the HTHP's performance maps. Based on the literature review and the CHEST system requirements, this range was selected to cover the expected operational range for most HTHPs used to deliver heat between 120 and 150 °C by recovering industrial waste heat between 60 and 100 °C. The inlet water to the subcooler is also an independent variable since it can come directly from the grid, from SP-TES, or as condensed water from any industrial process. The combination of these independent variables (full factorial of Table 5) produces 576 possible operating conditions.

Table 5
Range of the independent variables of HTHP's performance maps.

Variable	Range
n_{comp} [rps]	13.3, 18.3, 25
$T_{w,in,evap}$ [°C]	60, 70, 80, 100
$\Delta T_{w,evap}$ [K]	2, 4, 6
$T_{w,in,cond}$ [°C]	120, 130, 140, 150
$T_{w,in,subc}$ [°C]	20, 50, 75, 100

The four dependent variables, or key performance parameters selected for the HTHP's performance maps, are $P_{el,comp}$, $\dot{Q}_{cond}$, $\dot{Q}_{subc}$, and $\dot{Q}_{src}$. They represent the main inlet and outlet energy flow to/from the proposed HTHP. The idea behind this selection of variables is to ease the integration of such type of HTHP in dynamic models for steam generation or energy storage systems with predefined source (supply) and sink (demand) profiles. Moreover, the performance maps can be easily upscaled for different applications.

To simplify the extended performance maps, four correlations were derived for the main dependent variables as a function of the five independent variables. However, these correlations are not straightforward since there are potentially complicated interactions between the different independent variables. After generating the entire performance maps, they were converted to 3D surfaces, as shown in Fig. 14. Then, each response surface was bisected to different 2D figures to finally figure out the required relationships, not only between the dependent and independent variables, but also between the independent variables themselves.

The main tool used to derive the correlations is the "Regression" feature of the Microsoft Excel program. This powerful and easy-to-use tool presents all the relevant statistical data for the regression of a given data set. The main statistical parameters used to analyze the correlations are:

- Adjusted R^2: This value is used to quantify the quality of the correlation. This is achieved by indicating the variance of the dependent variable caused by the independent variable. A value close to one indicates that 100 % of the variation of the dependent variable is caused by the independent variable, and closer to zero indicates 0 %.
- Significance-F: This value represents the likelihood that the regression model is significant. The probability is presented as a fraction, and as such a value as low as possible is aimed for. A standard measurement with Significance-F to be deemed accurate is to be <5 %, and as such the target for this is Significance-F ≤ 0.05.
- Probability values (P-Values): These P-values are similar to the Significance F described above, but instead, these represent the probability that each coefficient of the regression is incorrect or doesn't have a significant effect on the results. Once again, a standard measurement used for good accuracy is <5 %, so the target value for acceptability is for all individual P-values ≤ 0.05.

With these parameters in mind, the following subsections illustrate a brief observation of the behavior of key performance parameters and the final set of performance correlations.

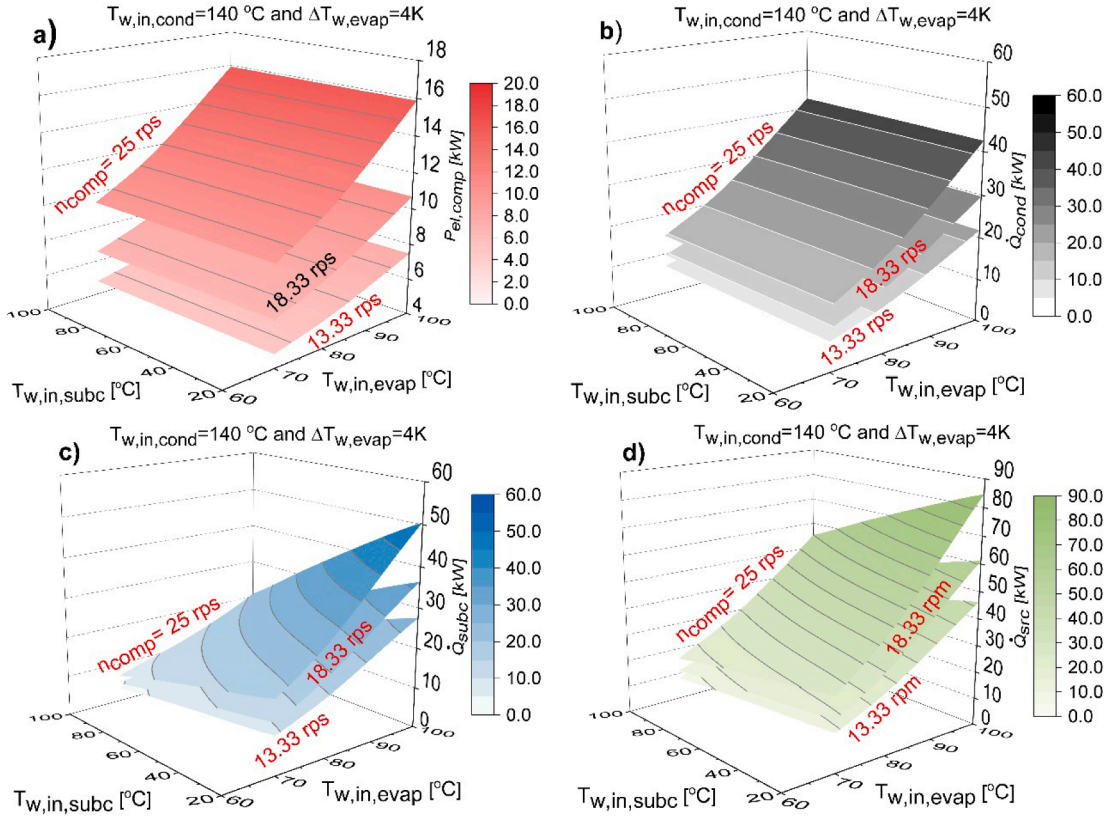

Fig. 14. HTHP's performance maps under constant $T_{w,in,cond}$ = 140 °C and $\Delta T_{w,evap}$ = 4 K where, (a) $P_{el,comp}$, (b) $\dot{Q}_{cond}$, (c) $\dot{Q}_{subc}$, and (d) $\dot{Q}_{src}$.

5.3.1. Compressor's electrical power consumption ($P_{el,comp}$)

The $P_{el,comp}$ correlation represents the main energy consumption by HTHP and significantly affects the HTHP's COP. The first stage in the development of the $P_{el,comp}$ correlation was to examine each independent variable's effect on the dependent variable by aids of 3D and 2D graphical representations. As seen in Fig. 14 a, $T_{w,in,subc}$ does not have a measurable effect on $P_{el,comp}$ under constant $T_{w,in,cond}$. On the contrary, $T_{w,in,evap}$ shows a clear quadratic relationship, and the variation of n_{comp} indicates a linear relationship with $P_{el,comp}$. Fixing n_{comp} shows a quadratic relationship between $P_{el,comp}$ and $T_{w,in,cond}$. $\Delta T_{w,evap}$ has a negligible impact on the four selected dependent variables.

Following these observations and after several attempts of trial-and-error, Eq. 17 shows the final correlation for the electrical power consumption relative to the compressor's speed.

$$\frac{P_{el,comp}}{n_{comp}} = C_0 + C_1 T_{w,in,evap}{}^2 + C_2 T_{w,in,evap} + C_3 n_{comp} + C_4 T_{w,in,cond}{}^2 + C_5 T_{w,in,cond} + C_6 T_{w,in,evap}{}^2 T_{w,in,cond} + C_7 T_{w,in,evap} T_{w,in,cond}{}^2 + C_8 T_{w,in,evap} T_{w,in,cond} \quad (17)$$

- Adjusted R^2 = 0.986
  Significance-F = 0
  Percentage of data within ± 5 % error bands = 88.1 %
  Percentage of data within ± 10 % error bands = 100 %

C_0	= 1.9317E + 00	(P-value = 1.81E-03)
C_1	= −9.6450E-04	(P-value = 1.57E-55)
C_2	= 6.1263E-02	(P-value = 1.69E-09)
C_3	= 3.6645E-03	(P-value = 1.15E-118)
C_4	= 4.9882E-04	(P-value = 5.80E-39)
C_5	= −7.7765E-02	(P-value = 2.72E-17)
C_6	= 7.9357E-06	(P-value = 8.51E-61)
C_7	= −5.8412E-06	(P-value = 9.80E-37)
C_8	= 2.5436E-04	(P-value = 2.70E-02)

5.3.2. Condenser's capacity ($\dot{Q}_{cond}$)

The $\dot{Q}_{cond}$ correlation represents the delivered latent heat for evaporating the water or melting the PCM at constant temperature. By comparing Fig. 14 a and b, it can be noticed that the curves of $\dot{Q}_{cond}$ show a similar trend as $P_{el,comp}$; therefore, similar relationships between the $\dot{Q}_{cond}$ independent variables could be expected, as for the $P_{el,comp}$ correlation. Based on this, the final proposed correlation for the $\dot{Q}_{cond}$is shown in Eq. (18).

$$\frac{\dot{Q}_{cond}}{n_{comp}} = C_0 + C_1 T_{w,in,evap}{}^2 + C_2 T_{w,in,evap} + C_3 n_{comp} + C_4 T_{w,in,cond}{}^2 + C_5 T_{w,in,cond} + C_6 T_{w,in,evap}{}^2 T_{w,in,cond}{}^2 + C_7 T_{w,in,evap} T_{w,in,cond}{}^2 + C_8 T_{w,in,evap} T_{w,in,cond} \quad (18)$$

- Adjusted R^2 = 0.999
  Significance-F = 0
  Percentage of data within ± 5 % error bands = 100 %
  Percentage of data within ± 10 % error bands = 100 %

C_0	= 5.5602E + 00	(P-value = 5.11E-14)
C_1	= 4.0559E-04	(P-value = 4.82E-32)
C_2	= −5.0830E-02	(P-value = 6.12E-08)
C_3	= 5.6388E-03	(P-value = 1.26E-155)
C_4	= 5.1190E-04	(P-value = 4.65E-24)
C_5	= −1.0167E-01	(P-value = 4.90E-18)
C_6	= 4.6512E-09	(P-value = 1.49E-02)
C_7	= −6.1403E-06	(P-value = 3.31E-18)
C_8	= 8.8111E-04	(P-value = 3.37E-10)

5.3.3. Subcooler's capacity ($\dot{Q}_{subc}$)

The $\dot{Q}_{subc}$ correlation represents the delivered sensible heat to preheat the liquid water before entering the condenser (Fig. 1); or to be stored in a sensible heat-thermal energy storage (SH-TES) system, as indicated in Fig. 2. This has an important impact on the system's COP as shown in Fig. 7. The $\dot{Q}_{subc}$ correlation is the most complicated since the subcooler works in a wide operating range, where SC_{subc} varies from 17 to 113 °C, and $\dot{m}_{w,subc}$ ranges from 0.014 to 0.2 kg/s. These conditions result in a capacity range from 1.4 to 52.2 kW. Unlike the previous dependent variables $P_{el,comp}$ and $\dot{Q}_{cond}$, the $\dot{Q}_{subc}$ has a strong linear dependency on $T_{w,in,subc}$, as seen in Fig. 14c. The other independent

variables have similar trends and relationships with $\dot{Q}_{subc}$ as in the case of $P_{el,comp}$ and $\dot{Q}_{cond}$. Eq. 19 summarizes the relationships of $\dot{Q}_{subc}$ with the independent variables.

$$\frac{\dot{Q}_{subc}}{n_{comp}} = C_0 + C_1 T_{w,in,evap}{}^2 + C_2 T_{w,in,evap} + C_3 T_{w,in,cond}{}^2 + C_4 T_{w,in,cond} + C_5 T_{w,in,subc} + C_6 T_{w,in,evap}{}^2 T_{w,in,cond} + C_7 T_{w,in,cond} T_{w,in,subc} + C_8 T_{w,in,evap} T_{w,in,subc} + C_9 T_{w,in,evap} T_{w,in,subc}{}^2 + C_{10} T_{w,in,evap}{}^2 T_{w,in,subc} \quad (19)$$

- Adjusted $R^2 = 0.999$
  Significance-F = 0
  Percentage of data within ± 5 % error bands = 96.4 %
  Percentage of data within ± 10 % error bands = 100 %

C_0	= 2.5411E-01	(P-value = 8.84E-02)
C_1	= 1.2703E-04	(P-value = 2.99E-24)
C_2	= −2.1913E-02	(P-value = 5.96E-32)
C_3	= −1.0776E-04	(P-value = 2.40E-40)
C_4	= 1.4777E-02	(P-value = 4.44E-13)
C_5	= −1.1561E-02	(P-value = 2.53E-28)
C_6	= 2.1518E-06	(P-value = 2.60E-255)
C_7	= 8.3885E-05	(P-value = 2.49E-140)
C_8	= 1.1844E-04	(P-value = 3.37E-06)
C_9	= −1.6302E-07	(P-value = 1.86E-33)
C_{10}	= −2.5383E-06	(P-value = 8.16E-50)

5.3.4. Source capacity ($\dot{Q}_{src}$)

The $\dot{Q}_{src}$ correlation represents the required waste heat to be recovered or upgraded by the HTHP. This is an important correlation to evaluate if the available waste heat is enough for the HTHP to satisfy a given demand. The same process is applied to drive a correlation of the $\dot{Q}_{src}$. The 3D map in Fig. 14 b shows that both $T_{w,in,subc}$ and n_{comp} have a linear relationship with $\dot{Q}_{src}$; while $T_{w,in,evap}$ has a quadratic one under constant $T_{w,in,cond}$. Under constant n_{comp}, varying the $T_{w,in,cond}$ shows a linear relationship with $\dot{Q}_{src}$. Based on these explanations, Eq. (20) shows the proposed correlation for $\dot{Q}_{src}$.

(continued on next column)

(continued)

$$\frac{\dot{Q}_{evap}}{n_{comp}} = C_0 + C_1 T_{w,in,evap}{}^2 + C_2 T_{w,in,evap} + C_3 T_{w,in,evap}{}^2 T_{w,in,subc} + C_4 T_{w,in,subc} + C_5 T_{w,in,evap} T_{w,in,cond} + C_6 T_{w,in,cond} + C_7 T_{w,in,cond} T_{w,in,subc} \quad (20)$$

- Adjusted $R^2 = 0.999$
  Significance-F = 0
  Percentage of data within ± 5 % error bands = 97.6 %
  Percentage of data within ± 10 % error bands = 100 %

C_0	= 1.5146E + 00	(P-value = 2.66E-34)
C_1	= 8.3103E-04	(P-value = 4.20E-297)
C_2	= −2.8429E-02	(P-value = 1.84E-49)
C_3	= −1.9334E-06	(P-value = 1.35E-307)
C_4	= −7.8424E-03	(P-value = 1.83E-33)
C_5	= −2.0008E-04	(P-value = 8.19E-61)
C_6	= −3.3919E-03	(P-value = 2.53E-04)
C_7	= 8.5533E-05	(P-value = 7.18E-60)

Fig. 15 shows how successfully the proposed performance correlations can represent the complete performance maps of the current HTHP, where 100 % of the data are within ± 10 % error bands.

6. Conclusions and recommendations

This work includes the design, manufacturing and experimental testing of a HTHP working with R-1233zd(E). The heat pump delivers both sensible and latent heat. Moreover, a simulation tool has been developed and validated with the experimental results. The heat pump configuration has been designed to be integrated into industrial applications where waste heat is available, and the heat demand requires temperatures up to 150 °C. This HTHP is of interest for applications with additional high temperature glide values requirements in the sink side (subcooler).

The experimental campaign consisted of 50 operating points where the heat source temperature ranged from 70 to 90 °C and the sink side (condenser) from 99 to 148.5 °C. The main conclusions of the current

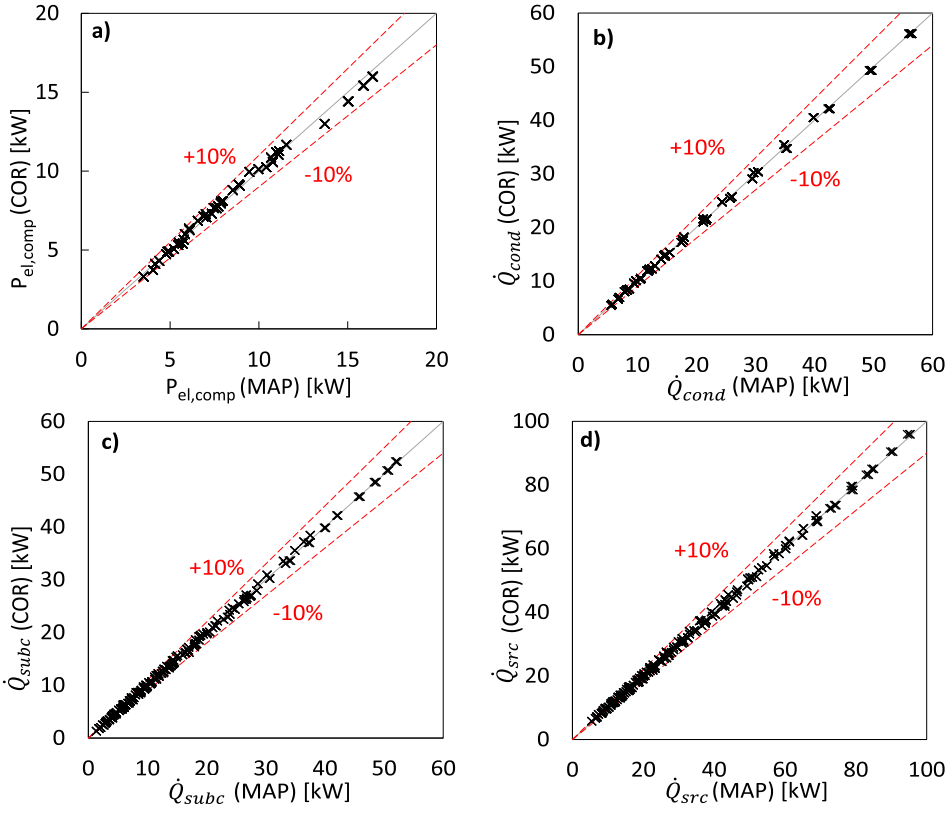

Fig. 15. Comparison of the proposed HTHP's performance correlations (COR) and maps (MAP) for (a) $P_{el,comp}$, (b) $\dot{Q}_{cond}$, (c) $\dot{Q}_{subc}$, and (d) $\dot{Q}_{src}$.

work are summarized as follows:

- The HTHP, for ΔT_{lift} = 60–67 K, shows COP values from 3 to 4. This was achieved thanks to the innovative configuration of the HTHP, which exploited a large part of sensible heat in the subcooler, substantially increasing the overall thermal output. In addition, the lower the water inlet temperature in the subcooler, the higher the total heating capacity and the COP values.
- The total heating capacity values (subcooler and condenser) ranged from 15.5 to 68.2 kW, with approximately 45—52 % of the total heat is delivered by the subcooler.
- The compressor's electric consumption ranged from 4.4 to 14.4 kW. The lower the heat source temperature and compressor speed, the lower the compressor consumption. The highest electricity consumption was observed under high heat source temperatures combined with high compressor speeds.
- The heat losses are considerably high, reaching values up to 18 % of the total heat generated by the HTHP. The heat losses were a result of the difference between the energy entering the system and the useful thermal energy produced.
- The heat losses were identified to happen via the oil cooling system, the liquid receiver and the compressor's enclosure. This had a negative impact on the overall efficiency of the HTHP. An adequate insulation on the liquid receiver and the compressor could reduce the heat losses. In addition, the heat from the oil cooling loop could be used in the heat source loop to further decrease the heat losses.
- Generally, the developed HTHP model can predict the performance parameters within ± 10 % error bands compared with experimental data. The validation study shows that the MAE values of the $P_{el,comp}$, $\dot{Q}_{cond}$, $\dot{Q}_{subc}$, and $\dot{Q}_{src}$ are ± 2.76 %, ±2.82 %, ±8.30 %, and ± 4.36 %, respectively.
- The extended performance maps (576 operating conditions) for the current HTHP were successfully summarized in four performance correlations (Eqs. 17—20) that depend only on four independent variables n_{comp}, $T_{w,in,evap}$, $T_{w,in,cond}$, and $T_{w,in,subc}$. They can predict 100 % of the performance map within ± 10 % error bands. These correlations can be integrated and easily upscaled for the simulation of the HTHP in different industrial applications.

In addition, the following points should be considered for a further development of such HTHPs:

- For water-cooled compressors, the heat transferred to the cooling loop should be somehow incorporated again into the system to decrease the total heat losses. Improving the compressor insulation could be an option to reduce the losses to the ambient, but the effect of this on the discharge temperature should be carefully investigated.
- Generally, single-piston compressors are not fully balanced and produce high-intensity vibrations, which could cause failures in the joints and fittings. The compressor's support bench and the rest of the HTHP components should be designed to absorb the forces generated by these vibrations.
- The fact that the compressor's motor is not in connection to the suction gases allows increasing the heat source temperature beyond the maximum temperature of the electric motor without any hazards on the motor's windings.
- To minimize the refrigerant solubility in the oil sump, the oil temperature should be maintained at least 10 K above the evaporation temperature.
- Liquid refrigerant can end in the compressor's oil from the return pipe of the oil separator, especially during cold start-ups. Proper oil separation system design and preheating of the oil separator's metallic surfaces is recommended.
- High-temperature compressors working with HFOs require special lubricants with high viscosity. These lubricants can lead to compressor faults during cold start-ups. Therefore, adequate lubricant design and preheating of the oil is recommended.
- The subcooler design must be carefully addressed considering the high ΔT values of both flows. Moreover, the water side of the subcooler must be designed for high pressure operation to avoid bubbles.
- The pipeline design of the HTHP, the positioning of high volume components, and the service ports must be studied. This can help to minimize the pressure losses, decrease the refrigerant charge in the system, and to facilitate fluid recovery and decommissioning phase.
- The derived performance correlations predict well the stand-alone behavior of the HTHP. They can be employed a black-box model to reproduce the behavior of the HTHP in different industrial applications. As future work, further exploitation of these correlations would be very interesting after integrating this HTHP prototype into an industrial process.

CRediT authorship contribution statement

Miguel Ramirez: . **Felipe Trebilcock Kelly:** Writing – original draft, Project administration, Investigation. **José L. Corrales Ciganda:** . **Jorge Payá:** . **Abdelrahman H. Hassan:** Writing – review & editing, Validation, Software, Investigation, Formal analysis.

Declaration of competing interest

The authors declare that they have no known competing financial interests or personal relationships that could have appeared to influence the work reported in this paper.

Data availability

The data that has been used is confidential.

Acknowledgment

This work has been partially funded by grant agreement No. 764042 (CHESTER project) of the European Union's Horizon 2020 research and innovation program.

The authors would like to dedicate this work to the memory of Prof. Dr. José Miguel Corberán for his outstanding efforts during the CHESTER project; his contributions, discussions, and suggestions were highly invaluable.

References

[1] C. Arpagaus, F. Bless, M. Uhlmann, J. Schiffmann, S.S. Bertsch, High temperature heat pumps: market overview, state of the art, research status, refrigerants, and application potentials, Energy 152 (2018) 985–1010.
[2] J. Jiang, B. Hu, R.Z. Wang, N. Deng, F. Cao, C.C. Wang, A review and perspective on industry high-temperature heat pumps, Renew. Sustain. Energy Rev. 161 (2022) 112106.
[3] K. Hamid, U. Sajjad, M. Ulrich Ahrens, S. Ren, P. Ganesan, I. Tolstorebrov, A. Arshad, Z. Said, A. Hafner, C.C. Wang, R. Wang, T.M. Eikevik, Potential evaluation of integrated high temperature heat pumps: a review of recent advances, Appl. Therm. Eng. 230 (2023) 120720.
[4] B. Zühlsdorf, Poulsen, Wilk, Rieberer and Arpagaus, IEA HPT Annex 58 High -Temperature Heat Pumps Task 1 – Technologies, 2023.
[5] Y. Jung, J. Oh, U. Han, H. Lee, A comprehensive review of thermal potential and heat utilization for water source heat pump systems, Energ. Build. 266 (2022) 112124.
[6] S. Wolf and M. Blesl, Model-based quantification of the contribution of industrial heat pumps to the European climate change mitigation strategy, Eceee Industrial Summer Study Proceedings, Vols. 2016-September, 2016.
[7] G. Kosmadakis, Estimating the potential of industrial (high-temperature) heat pumps for exploiting waste heat in EU industries, Appl. Therm. Eng. 156 (2019) 287–298.
[8] A. Marina, S. Spoelstra, H.A. Zondag, A.K. Wemmers, An estimation of the European industrial heat pump market potential, Renew. Sustain. Energy Rev. 139 (2021) 4.
[9] C. Arpagaus, J. Payá, A. Hassan and B. Stefan, Potential impact of industrial HTHPs on the european market, in: 3rd HTHP Symposium, Copenhagen, Denmark, 2022.

[10] L. Cozzi and T. Gül, Net Zero by 2050. A Roadmap for the Global Energy Sector, International Energy Agency, 2021.
[11] CHESTER, Compressed heat energy storage for energy from renewable sources, [Online]. <https://www.chester-project.eu/>.
[12] K.M. Adamson, T.G. Walmsley, J.K. Carson, Q. Chen, F. Schlosser, L. Kong, D. J. Cleland, High-temperature and transcritical heat pump cycles and advancements: a review, Renew. Sustain. Energy Rev. 167 (2022).
[13] C. Liu, W. Han, X. Xue, Experimental investigation of a high-temperature heat pump for industrial steam production, Appl. Energy 312 (2022) 118719.
[14] J. Navarro-Esbrí, A. Mota-Babiloni, Experimental analysis of a high temperature heat pump prototype with low global warming potential refrigerant R-1336mzz(Z) for heating production above 155 °C, Int. J. Thermofluids 17 (2023) 100304.
[15] T. Fleckl, M. Hartl, F. Helminger, K. Kontomaris and Pfaffl, Performance testing of a lab-scale high temperature heat pump with HFO-1336mzz-Z as the working fluid, in: European Heat Pump Summit 2015 (EHPS), Nuremberg, Germany, 2015.
[16] F. Helminger, M. Hartl, T. Fleckl, K. Kontomaris and J. Pfaffl, Hochtemperatur Wärmepumpen Messergebnisse einer Laboranlage mit HFO-1336MZZ-Z bis 160° C Kondensationstemperatur, in: 14. Symposium Energieinnovation, Graz, Austria, 2016.
[17] C. Arpagaus and S. Bertsch, Experimental results of HFO/HCFO refrigerants in a laboratory scale HTHP with up to 150 °C supply temperature, in: 2nd Conference on High Temperature Heat Pumps , Copenhagen, Denmark, 2019.
[18] G. Abi Chahla, Y. Beucher, A. Zoughaib, F. De Carlan, J. Pierucci, Transcritical Industrial Heat Pump Using HFO's for up to 150 °c Hot Air Supply, Montreal, Canada, 2019.
[19] Y. Zhang, Y. Zhang, X. Yu, J. Guo, N. Deng, S. Dong, Z. He, X. Ma, Analysis of a high temperature heat pump using BY-5 as refrigerant, Appl. Therm. Eng. 127 (2017) 1461–1468.
[20] N. Deng, X. Jing, R. Cai, J. Gao, C. Shen, Y. Zhang, H. Sui, Molecular simulation and experimental investigation for thermodynamic properties of new refrigerant NBY-1 for high temperature heat pump, Energ. Conver. Manage. 179 (2019) 339–348.
[21] R. Noack, Entwicklung einer Hochtemperatur-Waermepumpe für Nutztemperaturen über 120 °C, in: Deutsche Kaelte und Klimatagung, Kassel, Germany, 2016.
[22] Reissner, F. Reissner, Development of a Novel High Temperature Heat Pump System, Entwicklung eines neuartigen Hochtemperatur-Waermepumpensystems, PhD Thesis, Friedrich-Alexander Universitaet Erlangen-Nuernberg, 2015.
[23] D. Bobelin, A. Bourig, J. Pereux, Experimental results of a newly developed very high temperature industrial heat pump (140 °C) equipped with scroll compressors and working with a new blend refrigerant, in: International refrigeration and air conditioning conference, Purdue, USA, 2012.
[24] M. Verdnik, R. Rieberer, Influence of operating parameters on the COP of an R600 high-temperature heat pump, Int. J. Refrig 140 (2022) 103–111.
[25] T. Yamazaki, Y. Kubo, Development of a high-temperature heat pump. IEA heat pump centre newsletter, IEA (1985).
[26] D. Wu, J. Jiang, B. Hu, R.Z. Wang, Experimental investigation on the performance of a very high temperature heat pump with water refrigerant, Energy 190 (2020) 116427.
[27] P. d. Larminat, D. Arnou, P. Le Sausse, F. Clunet, J. L. Peureux, A high temperature heat pump using water vapor as working fluid, in: 1th IIR Gustav Lorentzen conference on natural refrigeration, Hangzhou, China, 2014.
[28] X. Sang, S.W. Xu, Z.Q. Yu, Research on NH3 screw high-temperature heat pump system with total heat recovery, Refrig. Air Cond. (2016) 41–44.
[29] W. Wu, W. Shi, J. Wang, B. Wang, X. Li, Experimental investigation on NH3-H2O compression-assisted absorption heat pump (CAHP) for low temperature heating under lower driving sources, Appl. Energy 176 (2016).
[30] G. Lee, B. Lee, J. Cho, H.-S. Ra, Y.-J. Baik, H.-K. Shin, Y.-S. Lee, Development of Steam Generation Heat Pump Through Refrigerant Replacement Approach, Rotterdam, Netherlands, 2017.
[31] X. Li, Y. Zhang, X. Ma, N. Deng, Z. Jin, X. Yu, W. Li, Performance analysis of high-temperature water source cascade heat pump using BY3B/BY6 as refrigerants, Appl. Therm. Eng. 159 (2019) 113895.
[32] A.H. Hassan, J.M. Corberán, M. Ramirez, F. Trebilcock-Kelly, J. Payá, A high-temperature heat pump for compressed heat energy storage applications: design, modeling, and performance, Energy Rep. 8 (2022) 10833–10848.
[33] C. Arpagaus, S. Bertsch, Experimental Comparison of HCFO and HFO R1224yd(Z), R1233zd(E), R1336mzz(Z), and HFC R245fa in a High Temperature Heat Pump up to 150 °C Supply Temperature, in: International Refrigeration and Air Conditioning Conference, Purdue, USA, 2021.
[34] M. Nilsson, H. N. Rislå, K. Kontomaris, Measured performance of a novel high temperature heat pump with HFO-1336mzz(Z) as the working fluid, in: 12th IEA Heat Pump Conference, Rotterdam, Netherlands, 2017.
[35] C. Arpagaus, F. Bless, S. Bertsch, P. Krummenacher, D. A. Florez-Orrego, E. A. Pina, F. Marechal, V. Stephane , S. Vesin, P. Achermann, C. Jansen, Integration of High-Temperature Heat Pumps in Swiss Industrial Processes (HTHP-CH), in: 14th IEA Heat Pump Conference, Chicago, USA, 2023.
[36] IEA(HPT), Annex 58, Task 1: Technologies–State of the art and ongoing developments for systems and components, 2022. [Online]. <https://heatpumpingtechnologies.org/annex58/task1/>.
[37] Oilon Group Oy, Oilon ChillHeat Industrial Heat Pumps, 2022. [Online]. <https://oilon.com/wp-content/uploads/2020/04/Oilon_ChillHeat_Industrial_Heat_Pumps.pdf>.
[38] Combitherm GmbH, Combitherm: High Temperature Heat Pumps, 2023. [Online]. <https://www.combitherm.de/en/produkte-und-loesungen/hochtemperaturwaermepumpen/>.
[39] Heaten, HeatBooster, 2023. <https://www.heaten.com/product/>.
[40] SPH GmbH, "Thermbooster Heat Pump," 2023. [Online]. Available: https://spheat.de/thermbooster/?lang=en.
[41] T. Hamacher, Industrial high temperature heat pump for steam and hot water production, in: 14th IEA Heat Pump Conference, Chicago, USA, 2023.
[42] A. Hassan, J. Payá, E. Navarro-Peris, Development and analysis of a high-temperature heat pump for steam generation using hydrocarbons as refrigerants, in: 15th IIR-Gustav Lorentzen Conference on Natural Refrigerants, Trondheim, Norway, 2022.
[43] T. Kaida, I. Sakuraba, K. Hashimoto and H. Hasegawa, "Experimental performance evaluation of heat pump-based steam supply system," IOP Conference Series: Materials Science and Engineering, vol. 90, p. 012076, 8 2015.
[44] A.H. Hassan, L. O'Donoghue, V. Sánchez-Canales, J.M. Corberán, J. Payá, H. Jockenhöfer, Thermodynamic analysis of high-temperature pumped thermal energy storage systems: Refrigerant selection, performance and limitations, Energy Rep. 6 (2020) 147–159.
[45] S. Klein, F. Alvarado, Engineering Equation Solver (version v10.643), F-Chart Software, Box, 2019.
[46] H. Jockenhöfer, W.D. Steinmann, D. Bauer, Detailed numerical investigation of a pumped thermal energy storage with low temperature heat integration, Energy 145 (2018) 665–676.
[47] C.A. Conditioners, Air conditioning, liquid chilling packages and heat pumps for space heating and cooling and process chillers with electrically driven compressors - Part 3: Test methods, DIN EN (2018) 14511–14513.
[48] E. W. Lemmon, I. H. Bell, M. L. Huber, M. O. McLinden, "NIST Standard Reference Database 23: Reference Fluid Thermodynamic and Transport Properties-REFPROP, NIST, 2018.
[49] Jcgm, 100: 2008 Evaluation of measurement data — Guide to the expression of uncertainty in measurement, Joint Committee for Guides in Metrology (2008).
[50] C. Arpagaus, R. Kuster, M. Prinzing, M. Uhlmann, E. Büchel, S. Frei, J. Schiffmann, S. Bertsch, High temperature heat pump using HFO and HCFO refrigerants-System design and experimental results, in: 25th IIR International Congress of Refrigeration, Montréal, Canada, 2019.
[51] I.U.I en Ingeniera Energética (IIE), IMST-ART: Simulation Tool to Assist the Selection, Design and Optimization of Refrigeration Equipment and Components, 2010. [Online]. <http://www.imst-art.com>. (Accessed 2023).
[52] J. M. Corberan, J. Gonzalvez, The matching problem on the modeling of vapor compression systems, in: International Refrigeration and Air Conditioning Conference, Purdue, 1998.
[53] B.S. Garbow, MINPACK-1, Subroutine Library for Nonlinear Equation System, 1984.
[54] M.J.D. Powell, Restart procedures for the conjugate gradient method, Math. Program. 12 (1) (1977) 241–254.
[55] J.M. Corberán, J. Gonzalvez, P. Fernández de Cordoba, Semiexplicit method for wall temperature linked equations (SEWTLE): a general finite-volume technique for the calculation of complex heat exchangers, Numer. Heat Transfer, Part B: Fund. 40 (1) (2001) 37–59.